Next, *in vitro* OGT assays using peptide arrays covering full-length H2B revealed peaks at 101–115 peptides in the carboxy (C)-terminal α-helix (αC)[12] (Supplementary Fig. 7). This peptide was found to bear only one moiety by matrix-assisted laser desorption/ionization–time of flight (MALDI–TOF)/MS (Supplementary Fig. 8). Indeed, substitutions of S112 and T122 to A significantly reduced *in vitro* GlcNAcylation by OGT (Fig. 1d), but not mutations in the amino (N)-terminal tail (Supplementary Fig. 9). On the basis of these data, we concluded that the conserved S112 was a GlcNAc site in H2B, whereas T122 might be needed for recognition by OGT (Fig. 1e, f).

With our newly developed antibody (Supplementary Fig. 10), H2B S112 GlcNAc was detected in histones of HeLa cells. Depletion of glucose from the media for 24 h induced deglycosylation with neither overt cell death (Fig. 2a and Supplementary Fig. 11) nor alteration in histone acetylation marks of cell state indicators (H3 K14, H3 K56, H4 K16)[13,14] (Supplementary Fig. 12). H2B S112 GlcNAc could be restored by re-treatment with glucose at physiological concentrations (Supplementary Fig. 13).

Because many histone modifications are orchestrated, we tested if H2B S112 GlcNAc influenced H2B K120 monoubiquitination because of their proximity. After glucose depletion, replenishment of glucose gradually increased global GlcNAcylation of proteins, followed by H2B S112 GlcNAc and H2B monoubiquitination (Fig. 2b, c). Their reciprocal modifications disappeared when OGT was knocked down (Fig. 2d and Supplementary Fig. 14). In addition, in the immunoprecipitates of H2B containing the S112A and T122A double mutations (H2B AA), no response of K120 monoubiquitination to extracellular glucose was detected (Fig. 2e and Supplementary Fig. 15). Conversely, GlcNAcylation of H2B S112 was observed, even when K120 was mutated to R (Fig. 2e). From these findings, we conclude that H2B K120 monoubiquitination is mediated, at least in part, through S112 GlcNAcylation.

As glucosamine, but not pyruvate, potentiated H2B S112 GlcNAc (Fig. 2f), it appeared that this GlcNAcylation step was dependent on the HBP. To clarify this point, two HBP inhibitors (DON and AZA) were tested (Supplementary Information). After glucose depletion from media, these inhibitors attenuated the effect of glucose in H2B S112 GlcNAcylation along with K120 monoubiquitination (Fig. 2f).

In yeast, it was previously shown that H2B K120 monoubiquitination was induced by carbohydrates by glycolysis[15]. To address this issue, inhibitors of both glycolysis and deGlcNAcylation were applied to assess the crosstalk between the two modifications. When the cells were treated with iodoacetate, which blocks glycolysis but not HBP[15], the glucose effects on histone modifications were impaired, whereas the additional treatment of an OGA inhibitor (PUGNAc) restored both H2B S112 and K120 monoubiquitination (Supplementary Fig. 16). These data support the notion that H2B S112 GlcNAc senses decreases in glucose levels below normal levels and acts to promote H2B monoubiquitination, a modification that is associated with active transcription. Together with the fact that OGT is absent in yeast[6], the present H2B S112 GlcNAc-dependent pathway appears to constitute a system capable of sensing nutritional states in metazoans.

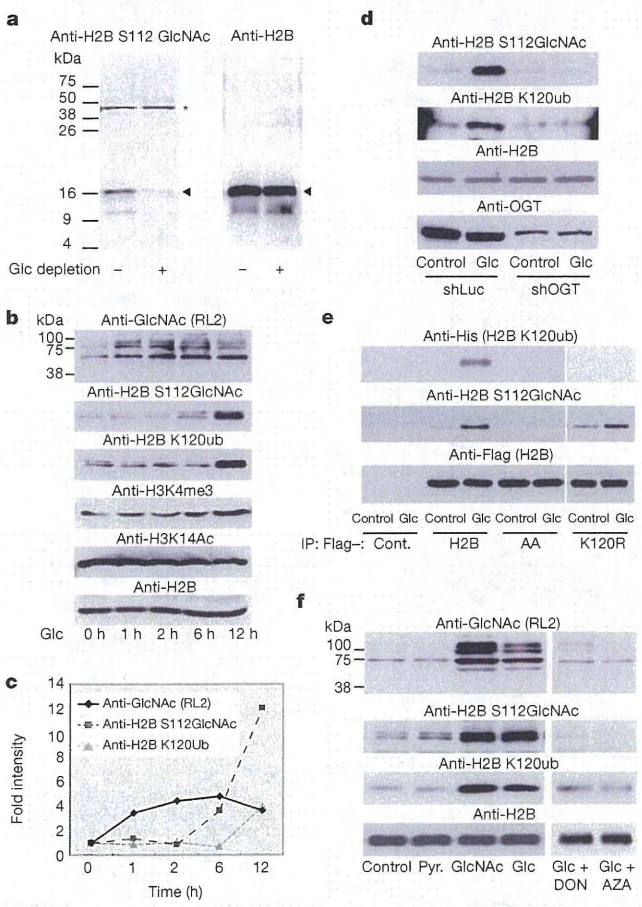

Figure 2 | H2B S112 GlcNAc is a glucose-responsive modification linked to K120 monoubiquitination (ub). **a**, Chromatin was prepared from HeLa cells cultured in media with or without 1 g l^{-1} glucose (Glc) for 24 h, and subjected to western blotting. Arrowheads show the indicated proteins. Asterisks indicate non-specific band. **b**, **c**, After 24 h Glc depletion, chromatin samples were prepared from HeLa cells treated with 4.5 g l^{-1} Glc for the indicated time. The intensities of the western blotting bands (**b**) were quantified (**c**). **d**, **e**, The effects of OGT knockdown (**d**) or H2B mutations (**e**) on H2B modifications after Glc replenishment. **f**, Western blotting analysis of the H2B modifications in HeLa cells that were cultured in DMEM without Glc (Cont.), or supplemented with 1 mM pyruvate (Pyr.), 10 mM GlcNAc or 4.5 g l^{-1} Glc with or without HBP inhibitors, 6-diazo-5-oxo-L-norleucine (100 μM, DON) or azaserine (100 μM, AZA).

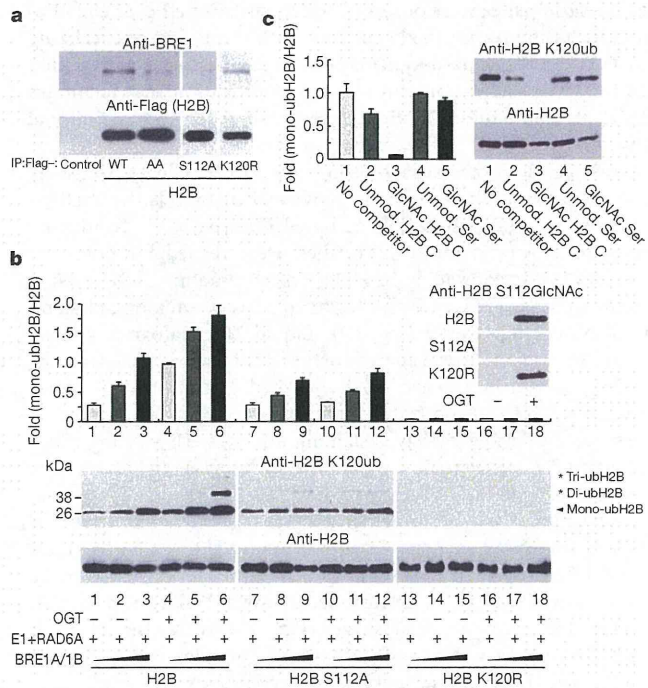

Figure 3 | GlcNAcylation at S112 facilitates ubiquitination at K120 in H2B. **a**, Western blotting analysis of the interaction of H2B mutants with BRE1A. **b**, **c**, *In vitro* monoubiquitination assay with GlcNAcylated H2B (**b**), or in the presence of competitor peptides (**c**). H2B was GlcNAcylated *in vitro* (**b**, top right), and the reactants were subsequently ubiquitinated by H2B monoubiquitination ligase. The reaction was performed with the indicated competitor peptides (0.25 μg ml^{-1}) (**c**). H2B K120 monoubiquitination was detected by western blotting (**b**, bottom; **c**, right) and quantified (**b**, top; **c**, left). Error bars, means and s.d. ($n = 3$).

The terminal GlcNAc of polysaccharides reportedly serves as a recognition moiety for E3 monoubiquitination ligase[16]. Therefore, we proposed that H2B S112 GlcNAc affected K120 monoubiquitination by the BRE1A/1B complex[17]. Flag-tagged H2B, but not AA or S112A, was co-immunoprecipitated with BRE1A (Fig. 3a). This association was observed in the presence of physiological levels of glucose in the media, and BRE1A was bound to H2B S112 GlcNAc (Supplementary Fig. 17). We then assessed how the GlcNAcylation of H2B influenced its *in vitro* ubiquitination by E1, RAD6A (E2) and the BRE1A/1B complex (E3). Although H2B K120 could be substantially ubiquitinated only by the ligases (Supplementary Fig. 18), GlcNAcylation of H2B promoted subsequent H2B ubiquitination, but not its S112A mutant (Fig. 3b). Likewise, ubiquitination was significantly attenuated by the presence of an H2B-S112-GlcNAcylated peptide, but not by either the unmodified control peptide or by GlcNAcylated serine (Fig. 3c). On the basis of these results, we conclude that the GlcNAc moiety at H2B S112 may anchor H2B monoubiquitination ligase.

To illustrate the role of H2B S112 GlcNAc in chromatin regulation, its location was visualized on fly polytene chromosomes. H2B S112 GlcNAc was detected widely in euchromatin, and, as anticipated, its signal disappeared in an OGT-disrupted fly, sxc^{1}/sxc^{78} (Supplementary Fig. 19). H2B S112 GlcNAc overlapped with H3K4 me2 more than with H3K9 me2 or H3K27 me3 (Fig. 4a). Similarly, in immunostained HeLa cells, H2B S112 GlcNAc sites appeared exclusively in 4′,6-diamidino-2-phenylindole (DAPI)-poor areas (Supplementary Fig. 20). Thus, H2B S112 GlcNAc probably accumulates in active chromatin rather than inactive chromatin.

To determine the precise loci of H2B S112 GlcNAc in HeLa cells, we performed chromatin immunoprecipitation (ChIP) and high-throughput sequencing (ChIP-seq). We confirmed ChIP quality by enrichments of H2B GlcNAc as well as H3K4 me2 and H2B K120 monoubiquitination, but neither H3K9 me2 nor H3K27 me3 (Supplementary Fig. 21). A total of 47,375 peaks were found widely distributed over the genome (Supplementary Fig. 22). However, H2B S112 GlcNAc peaked near transcription start sites (TSS), whereas the distribution decreased at transcription termination sites (TTS) (Fig. 4b), suggesting that it correlated with transcriptional regulation. To test this assumption, the activities of genes harbouring H2B S112 GlcNAc near TSS were estimated by microarray analysis (Supplementary Table 2). The average profiles near TSS significantly correlated with gene activity (Fig. 4c). Moreover, the expression levels of the 1,299 genes were reliably measured, and 1,021 genes showed high expression (Supplementary Fig. 23a and Supplementary Table 3b). Moreover, gene ontology analysis revealed that there was an association of the genes harbouring H2B S112 GlcNAc to cellular metabolic processes (Supplementary Fig. 23b and Supplementary Table 3c).

Next, we analysed the genome-wide overlap of H2B S112 GlcNAc with K120 monoubiquitination. A total of 44,158 peaks of H2B K120 monoubiquitination were detected, and their average profiles near TSS were similar to those profiles of H2B S112 GlcNAc (Supplementary

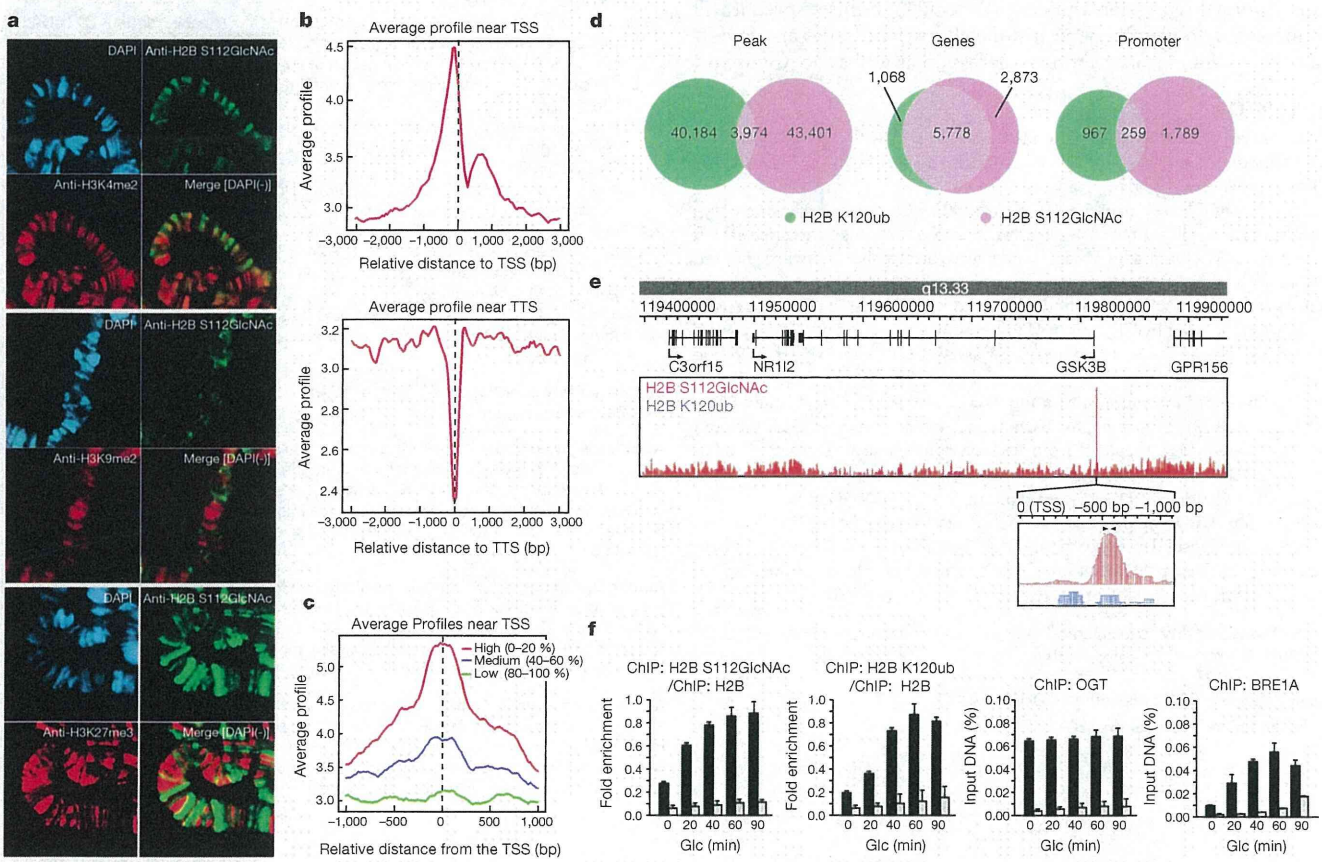

Figure 4 | GlcNAcylated H2B is associated with transcribed genes. **a**, Polytene staining with α-H2B S112 GlcNAc (green) and DAPI (blue) along with α-H3K4me2 (red, top), α-H3K9me2 (red, middle) or α-H3K27me3 (red, bottom). **b–e**, ChIP-seq analysis of the H2B S112 GlcNAc and K120 monoubiquitination. The distributions of H2B S112 GlcNAc were averaged near TSS (top) and TTS (bottom) (**b**). The average profiles of H2B S112 GlcNAc near TSS were calculated based on the associated gene activities (**c**). Venn diagrams showing overlap of the peaks (**d**, left), and the genes (**d**, middle) and the promoter (**d**, right) harbouring the modifications. The ChIP-seq profile surrounding the *GSK3B* gene (**e**). Arrowhead, position of qPCR primer. **f**, ChIP–qPCR validation in the GSK3B promoter. After Glc depletion, the control HeLa cells (black bar) and the OGT-knockdown cells (white bar) were replenished with Glc for 24 h. Then, the cells were subjected to ChIP with the indicated antibody and qPCR analysis. Error bars, means and s.d. ($n = 3$).

Fig. 24). Among the H2B K120 monoubiquitination peaks, nearly 10% (3,974 peaks) overlapped with H2B S112 GlcNAc peaks (Fig. 4d, left), and this evaluation was confirmed by a sequential ChIP–reChIP assay (Supplementary Fig. 25). Although 5,778 genes (66.8% of H2B S112 GlcNAc and 84.4% of K120 monoubiquitination) were found at the same loci (Fig. 4d, middle, and Supplementary Table 3d), 259 genes were identified when the two peaks were compared only within the promoters (Fig. 4d, right). The results of the ChIP-seq analysis were validated by ChIP–quantitative PCR (qPCR) assessment for the glycogen synthase kinase 3β (*GSK3B*) gene (Fig. 4e, f). These findings suggest that at several H2B S112 GlcNAc sites, it aids H2B monoubiquitination ligase recruitment whereas at others additional or different factors may be operational.

Here we provide evidence that histone GlcNAcylation is a post-translational modification correlated with active transcriptional events, and is responsive to serum glucose levels and/or cellular energy states in certain cell types (Supplementary Fig. 1). Using an antibody that specifically recognizes the S112 GlcNAc moiety of endogenous H2B, H2B was shown to serve as an OGT substrate. We have focused on the role of H2B S112 GlcNAcylation in gene regulation (Supplementary Fig. 1). Genome-wide analysis revealed that H2B S112 GlcNAc was frequently located near transcribed genes, suggesting that histone GlcNAcylation facilitates transcription of the genes. This idea is supported by previous reports that transcriptional output driven by several transcription factors is co-activated by OGT[9,18–20]. However, recent papers reported that *Drosophila* OGT is itself a polycomb group protein[8,21], and that many *O*-GlcNAcylated factors are involved in transcriptional repression and gene silencing[7,8]. In this respect, it will be interesting to identify other histone glycosylation sites and investigate their roles in transcriptional repression as well as activation.

METHODS SUMMARY

Plasmids and cell culture. All plasmids were generated with standard protocols (see Methods). Retrovirus production, infection and sorting of the infected cells followed previously reported protocols[9].

Purification of GlcNAc proteins from chromatin. Chromatin pellets were prepared from HeLa cells as previously described[22]. GlcNAc proteins were enriched with α-*O*-GlcNAc (RL2) antibody (Abcam) immobilized on Dynabeads (Invitrogen), and released with GlcNAc-*O*-serine.

Generation of monoclonal antibody. The synthetic H2B S112 GlcNAc peptide (CKHAV S(GlcNAc) EGTK) was used to immunize mice. The hybridomas were selected by enzyme-linked immunosorbent assay (ELISA) and western blotting analysis.

***In vitro* OGT and monoubiquitination assays.** Flag–OGT, Flag–E1, and Flag–BRE1A/BRE1B were purified by baculoviral systems, whereas histones and 6 × His-RAD6A were prepared from bacteria as previously reported[17,23]. H2B was incubated with OGT or H2B monoubiquitination ligases *in vitro*, and its modification was detected by western blotting as previously reported[9,23].

ChIP-seq and ChIP–qPCR. ChIP and ChIP-seq library construction was performed as previously described[24,25], and the libraries were sequenced to 50 base pairs (bp) with Hiseq2000 (Illumina). The fragments of interest in the libraries were quantified with specific promoter sets (Methods) by qPCR.

Full Methods and any associated references are available in the online version of the paper at www.nature.com/nature.

Received 16 July 2010; accepted 20 October 2011.
Published online 27 November 2011.

1. Strahl, B. D. & Allis, C. D. The language of covalent histone modifications. *Nature* **403,** 41–45 (2000).
2. Kouzarides, T. Chromatin modifications and their function. *Cell* **128,** 693–705 (2007).
3. Li, B., Carey, M. & Workman, J. L. The role of chromatin during transcription. *Cell* **128,** 707–719 (2007).
4. Berger, S. L. The complex language of chromatin regulation during transcription. *Nature* **447,** 407–412 (2007).
5. Hart, G. W., Housley, M. P. & Slawson, C. Cycling of O-linked β-*N*-acetylglucosamine on nucleocytoplasmic proteins. *Nature* **446,** 1017–1022 (2007).
6. Love, D. C. & Hanover, J. A. The hexosamine signaling pathway: deciphering the 'O-GlcNAc code'. *Sci. STKE* **2005,** re13 (2005).
7. Yang, X., Zhang, F. & Kudlow, J. E. Recruitment of O-GlcNAc transferase to promoters by corepressor mSin3A: coupling protein O-GlcNAcylation to transcriptional repression. *Cell* **110,** 69–80 (2002).
8. Gambetta, M. C., Oktaba, K. & Muller, J. Essential role of the glycosyltransferase sxc/Ogt in polycomb repression. *Science* **325,** 93–96 (2009).
9. Fujiki, R. *et al.* GlcNAcylation of a histone methyltransferase in retinoic-acid-induced granulopoiesis. *Nature* **459,** 455–459 (2009).
10. Wang, Z. *et al.* Extensive crosstalk between O-GlcNAcylation and phosphorylation regulates cytokinesis. *Sci. Signal.* **3,** ra2 (2010).
11. Sakabe, K., Wang, Z. & Hart, G. W. β-N-acetylglucosamine (O-GlcNAc) is part of the histone code. *Proc. Natl Acad. Sci. USA* **107,** 19915–19920 (2010).
12. Luger, K. *et al.* Crystal structure of the nucleosome core particle at 2.8 Å resolution. *Nature* **389,** 251–260 (1997).
13. Das, C., Lucia, M. S., Hansen, K. C. & Tyler, J. K. CBP/p300-mediated acetylation of histone H3 on lysine 56. *Nature* **459,** 113–117 (2009).
14. Dang, W. *et al.* Histone H4 lysine 16 acetylation regulates cellular lifespan. *Nature* **459,** 802–807 (2009).
15. Dong, L. & Xu, C. W. Carbohydrates induce mono-ubiquitination of H2B in yeast. *J. Biol. Chem.* **279,** 1577–1580 (2004).
16. Yoshida, Y. *et al.* E3 ubiquitin ligase that recognizes sugar chains. *Nature* **418,** 438–442 (2002).
17. Kim, J. *et al.* RAD6-Mediated transcription-coupled H2B ubiquitylation directly stimulates H3K4 methylation in human cells. *Cell* **137,** 459–471 (2009).
18. Dentin, R. *et al.* Hepatic glucose sensing via the CREB coactivator CRTC2. *Science* **319,** 1402–1405 (2008).
19. Chikanishi, T. *et al.* Glucose-induced expression of MIP-1 genes requires O-GlcNAc transferase in monocytes. *Biochem. Biophys. Res. Commun.* **394,** 865–870 (2010).
20. Jackson, S. P. & Tjian, R. O-glycosylation of eukaryotic transcription factors: implications for mechanisms of transcriptional regulation. *Cell* **55,** 125–133 (1988).
21. Sinclair, D. A. *et al. Drosophila* O-GlcNAc transferase (OGT) is encoded by the Polycomb group (PcG) gene, super sex combs (sxc). *Proc. Natl Acad. Sci. USA* **106,** 13427–13432 (2009).
22. Sawatsubashi, S. *et al.* A histone chaperone, DEK, transcriptionally coactivates a nuclear receptor. *Genes Dev.* **24,** 159–170 (2009).
23. Fujiki, R. *et al.* Ligand-induced transrepression by VDR through association of WSTF with acetylated histones. *EMBO J.* **24,** 3881–3894 (2005).
24. He, H. H. *et al.* Nucleosome dynamics define transcriptional enhancers. *Nature Genet.* **42,** 343–347 (2010).
25. Minsky, N. *et al.* Monoubiquitinated H2B is associated with the transcribed region of highly expressed genes in human cells. *Nature Cell Biol.* **10,** 483–488 (2008).

Supplementary Information is linked to the online version of the paper at www.nature.com/nature.

Acknowledgements We thank A. Miyajima, S. Saito and N. Moriyama for experimental support, and M. Yamaki for manuscript preparation. We also thank Y. Maekawa, J. Seta and N. Iwasaki for support with MS. This work was supported in part by The Naito Foundation, the Astellas foundation (to R.F.), the Ministry of Education, Culture, Sports, Science and Technology (MEXT) and the Japan Society for the Promotion of Science (to R.F. and S.K.).

Author Contributions S.K. planned the study with H.K.; R.G.R. and M.B. provided support and general guidance; R.F. designed the study and performed the experiments with H.S. (α-*O*-GlcNAc purification), A.Y. (LC–MS/MS), W.H. (*O*-GlcNAc site mapping), T.C. (*in vitro* OGT assay), S.I. (*Drosophila* analysis), Y.I., H.H.H. (ChIP-seq), F.O., J.K. (*in vitro* monoubiquitination assay), K.I. and J.K (microarray).

Author Information Reprints and permissions information is available at www.nature.com/reprints. The authors declare no competing financial interests. Readers are welcome to comment on the online version of this article at www.nature.com/nature. Correspondence and requests for materials should be addressed to S.K. (uskato@mail.ecc.u-tokyo.ac.jp).

METHODS

Plasmids and retroviruses. Complementary DNAs (cDNAs) of N-terminally Flag-tagged H2B and its mutant were subcloned into pcDNA3 (Invitrogen). A series of H2B point mutants were subcloned into the pET3 vector (Novagen). shRNA sequences targeting hOGT (5′-GCACATAGCAATCTGGCTTCC-3′) and *Renilla* luciferase (5′-TGCGTTGCTAGTACCAAC-3′, as a control) were inserted into the pSIREN-RetroQ-ZsGreen vector (Clontech). For retroviral production, the constructed shRNA vectors were transfected into PLAT-A cells. The virus contained in the medium was used for infection.

Generation of stable cell lines. To generate OGT-KD cells by retroviral infection, 10^6 cells were plated in 60 mm culture dishes, treated with 3 ml of retroviral cocktail (1 ml of the prepared retroviral solution plus 2 ml of DMEM with 10% FBS and 8 μg ml^{-1} polybrene), then cultured for another 48 h. A FACSVantage (BD) sorter was used to isolate the retrovirally transduced, enhanced green fluorescent protein (eGFP)-positive cells, as previously described[9]. To generate the cells stably expressing Flag-tagged constructs, HeLa cells were transfected with the pcDNA vectors encoding the Flag-tagged H2B or the AA mutant. The cells containing the integrated vectors were selected by exposure to 0.5 mg ml^{-1} G418.

Generation of monoclonal antibody. H2B S112 GlcNAc peptide (CKHAV S(GlcNAc) EGTK) was synthesized (MBL Institute) and used as an antigen (Operon Biotechnologies). The hybridomas were briefly screened using ELISA with the GlcNAc peptide, and finally selected by immunoblot analysis with the *in vitro* GlcNAcylated H2B.

Antibodies. Antibodies were obtained as follows: α-Flag M2 agarose (Sigma), α-H2A, α-H2B, α-H3, α-H4 (Abcam), α-H2B K120 monoubiquitination (Upstate), α-GlcNAc (RL2 or CTD110.6) (Abcam), α-OGT (Sigma), α-Flag (Sigma) and α-RNF20/BRE1A (Bethyl).

Purification and identification of GlcNAc proteins. The α-*O*-GlcNAc-immobilized beads were prepared with 15 μg α-*O*-GlcNAc (RL2) antibody and 0.5 ml of Dynabeads M-280 sheep α-mouse IgG (Invitrogen) according to the manufacturer's instructions. Chromatin extracts from HeLa cells (0.5 g protein) were prepared essentially as previously described[22]. In brief, the chromatin pellet, which consisted of residual material from the nuclear extract preparation with buffers supplemented with 1 mM streptozotocin (STZ), was re-suspended with micrococcal nuclease (MNase) buffer (20 mM Tris-HCl, 1 mM $CaCl_2$, 2 mM $MgCl_2$, 0.1 M KCl, 0.1% (v/v) Triton-X, 0.3 M sucrose, 1 mM DTT, 1 mM benzamidine, 0.2 mM PMSF, 1 mM STZ, pH 7.9). After addition of 3 U ml^{-1} MNase, the samples were incubated for 30 min at room temperature with continuous homogenization and the reaction was stopped by adding 5 mM EGTA and 5 mM EDTA. After centrifugation at 2,000*g* for 30 min at 4 °C, the supernatant (chromatin extract) was used for the following purification steps. The chromatin extracts were passed through a WGA agarose column (Vector). The flow-through fraction was further mixed with α-*O*-GlcNAc-immobilized beads and rotated for 8 h at 4 °C. After three washes with buffer D (20 mM Tris-HCl, 0.2 mM EDTA, 5 mM $MgCl_2$, 0.1 M KCl, 0.05% (v/v) NP-40, 10% (v/v) glycerol, 1 mM DTT, 1 mM benzamidine, 0.2 mM PMSF, 1 mM STZ, pH 7.9), glycoproteins were eluted twice with buffer D plus 0.4 mg ml^{-1} GlcNAc-*O*-serine (MBL) (elutions 1 and 2) and finally with 0.1 M glycine-HCl (pH2.0) (elution 3). Eluted proteins were desalted by methanol–chloroform precipitation, digested with trypsin (Promega) then loaded on the automated LC–MS/MS system, which was assembled with Zaplous nano-LC (AMR) plumbed with a reverse-phase C18 electrospray ionization (ESI) column (LC assist) and a Fiinigan LTQ ion-trap mass spectrometer (Thermo). The LC–MS/MS data were processed using Thermo BioWorks (Thermo) and SEQUEST (Thermo) for protein identification. The list of the identified proteins was further analysed by using the 'gene functional classification tool' in DAVID bioinformatics resources 6.7 (http://david.abcc.ncifcrf.gov/).

Recombinant proteins. Preparation of recombinant proteins was performed as previously reported[9,23]. Recombinant Flag–OGT, Flag–E1, Flag–BRE1A/B complexes were isolated by baculovirus expression and immunoprecipitation-based purification with α-Flag M2 agarose (Sigma). Recombinant 6 × His-RAD6A was expressed in bacteria and partly isolated with a HIS-Select Nickel Affinity Gel (Sigma). The eluate was diluted 1:20 with BC0 (20 mM HEPES, 0.2 mM EDTA, 10% (v/v) glycerol, pH 7.9), and fractionated with a Resource Q column (GE Healthcare) using a linear gradient (0–0.5 M KCl) method. Preparation of recombinant *Xenopus* histone H2B and its mutants was performed as previously described[9,23].

***In vitro* GlcNAcylation assay (autoradiographic analysis).** Recombinant Flag–OGT protein (0.5 μg) was incubated with 0.5 μg of recombinant histone and 0.2 mM (0.2 μCi) UDP-[^{3}H]GlcNAc (PerkinElmer) in a 25 μl reaction (50 mM Tris-HCl, 12.5 mM $MgCl_2$, 1 mM DTT, pH 7.5) for 24 h at 37 °C. The reaction was resolved with SDS–PAGE, blotted onto a polyvinylidene difluoride (PVDF) membrane, then subjected to autoradiography after spraying EN^{3}HANCE (NEN Lifescience).

***In vitro* GlcNAcylation assay (MS analysis).** Recombinant histones (1 μg) or recombinant histone octamers assembled *in vitro* (1 μg) were GlcNAcylated by recombinant Flag–OGT in 25 μl reactions (50 mM Tris-HCl, 2 mM UDP-GlcNAc, 12.5 mM $MgCl_2$, 1 mM DTT, pH 7.5) for 24 h at 37 °C. The reactions were directly subjected to a nano-LC ESI–TOF mass spectrometer system, which was assembled with a 1100 nanoLC (Agilent) plumbed with a ZORBAX 300SB-C18 column (Agilent) and micrOTOF (Bruker). Or, the reactions were digested with trypsin (Promega) and subjected to purification of glycopeptides with an MB-LAC WGA kit (Bruker). The enriched glycopeptides were loaded on the nano-LC ESI–ETD ion-trap mass-spectrometer system, which was assembled with the Agilent HP1200 Nano (Agilent) plumbed with ZORBAX 300SB-C18 (Agilent) and amaZon ETD (Bruker).

***In vitro* monoubiquitination assay.** GlcNAcylated histones (1 μg) were ubiquitinated with the E1 (0.1 μg), RAD6 (0.2 μg), BRE1 complex (0.5 μg), ubiquitin (3 μg) in 50 mM Tris (pH7.9), 5 mM $MgCl_2$, 4 mM ATP at 37 °C for 24 h.

ChIP-seq and ChIP–qPCR. ChIP and ChIP-seq libraries were constructed as previously described[24,25]. For ChIP-seq analysis, the libraries were sequenced to 50 bp with Hiseq2000 (Illumina). For ChIP–qPCR analysis, the fragments of interest in the libraries were quantified with Thermal Cycler TP800 (TAKARA) and SYBR Premix Ex Taq II (Takara). The qPCR primer sets for the *GSK3B* gene were 5′-TGCAAGCTCTCAGACGCTAA-3′ and 5′-CTCATTTCTCATGGGCG TTT-3′.

Journal of Steroid Biochemistry & Molecular Biology 127 (2011) 301–306

Contents lists available at ScienceDirect

Journal of Steroid Biochemistry and Molecular Biology

journal homepage: www.elsevier.com/locate/jsbmb

Androgen dependent transcription of a mouse prostatic protein gene, PSP94: Involvement of estrogen receptors☆

Nariaki Fujimoto[a,*], Shigeyuki Kitamura[b], Jun Kanno[c]

[a] Department of Disease Model, Research Institute for Radiation Biology and Medicine (RIRBM), Hiroshima University, 1-2-3 Kasumi, Minami-ku, Hiroshima 734-8553, Japan
[b] Faculty of Pharmacology, Nihon Pharmaceutical University, 10281 Komuro, Inamachi, Kita-ashikaga-gun, Saitama 362-0806, Japan
[c] Division of Toxicology, Biological Safety Research Center, National Institute of Health Sciences, Kamiyoga 1-18-1, Setagaya-ku, Tokyo 158-8501, Japan

ARTICLE INFO

Article history:
Received 20 April 2011
Received in revised form 20 July 2011
Accepted 2 August 2011

Keywords:
PSP94
Androgen dependent transcription
ARE
Androgen receptor
Estrogen receptor

ABSTRACT

Prostatic secretory protein 94 (PSP94) is a prostatic protein found in both humans and rodents. As with other prostatic proteins, expression of this protein is regulated by androgens. In order to understand the androgen-responsive transcriptional regulation mechanisms involved, the present study aimed to identify and characterize the promoter activity of the gene. The 5′flanking (5′f) region of mouse PSP94 (mPSP94) gene was cloned and introduced into a vector upstream of the luciferase reporter gene. A Chinese hamster ovarian cell line, CHO, and a human prostate adenocarcinoma cell line, LNCaP, were transiently transfected with our reporter constructs along with an androgen receptor expression vector, and treated with dihydrotestosterone. Reporter gene assay revealed that the 5′f region of mPSP94 gene was indeed responsible for the androgen-dependent transcription. Subsequent deletion and mutation analysis indicated that the androgen responsive element (ARE)-like sequence at position −93 from the transcription start site was primarily responsible for androgen dependency. Interestingly, when estrogen receptor (ER) α was co-transfected, the androgen-dependent transcription was substantially increased. However, ERα-dependent enhancement of androgen responses was not observed when estrogen responsive element (ERE)-like motifs of the promoter region were deleted. Administration of estrogen did not influence the enhancement associated with ERα, although an anti-estrogen suppressed such effects. Collectively, these data suggest that the androgen-dependent transcription of the mPSP94 gene was co-regulated/modulated by the presence of ERα via ERE-like motifs.

1. Introduction

Prostatic secretory protein 94 (PSP94), or β-microseminoprotein, is one of the major proteins along with PSA (prostate specific antigen) and PAP (prostatic acid phosphatase) that are secreted by the human prostate gland [1–3]. PSP94 is also secreted in abundance by the rodent prostate although the composition of prostatic proteins differ significantly between rodents and primates [4,5]. The rodent prostate consists of anatomically separate prostatic lobes including ventral, lateral, dorsal and anterior lobes. PSP94 is known to be highly expressed in dorsal and lateral regions of the rat prostate but localized to ventral and dorso-lateral prostatic lobes in mice. PSP94 may function as an immunoglobulin binding protein and is involved in the regulation of immune response in the female reproductive tract [6]. In addition, PSP94 is known to inhibit motility of sperm and the acrosome reaction [7]. PSP94 homologues have been identified in several other mammals and non-mammalian species including ostrich and Japanese viper [8]. The PSP94 family of proteins share ten highly conserved cysteine residues.

The expression of PSP94 is regulated by androgens, in a manner similar to other prostatic proteins such as human PSA and rat probasin [9–11]. In the human PSA gene, an androgen-responsive element (ARE) motif capable of inducing transcription in response to androgens via androgen receptors (AR) was identified in the promoter region at position −156 upstream of the transcriptional starting site [12]. Another functional ARE was additionally identified at approximately −4 kbp [13]. In the rat probasin gene, two functional AREs were identified in the 5′flanking (5′f) region. Interestingly, these were androgen selective AREs rather than responsive to androgens and glucocorticoids [14,15]. In the case of PSP94, it was demonstrated that the 5′f region of the mouse PSP94 (mPSP94) gene exhibited promoter activity which conferred prostatic-specific expression in transgenic mice [16]. However, the androgen-responsive transcription mechanism responsible for such promoter activity has yet to be identified.

☆ Grant support: Grant-in-Aid (H19-kagaku-Ippan-003) from the Ministry of Health, Labor and Welfare, Japan; Grant-in-Aid (#17510046) from the Ministry of Education, Culture, Sports, Science and Technology, Japan.

* Corresponding author. Tel.: +81 82 257 5820; fax: +81 82 256 7107.
E-mail address: nfjm@hiroshima-u.ac.jp (N. Fujimoto).

0960-0760/$ – see front matter © 2011 Elsevier Ltd. All rights reserved.
doi:10.1016/j.jsbmb.2011.08.001

At position −93 from the transcription start site of mPSP94 gene, there is an ARE-like sequence, TACCTAnnnTGTTCT that contains half site of consensus ARE, TGTTCT. We demonstrated that this site is indeed a functional ARE for androgen-dependent transcription in the present study. Interestingly, the promoter region also contains sequences similar to estrogen responsive element (ERE) which enhance androgen-dependent promoter activity of the gene in the presence of the estrogen receptor (ER) α.

2. Materials and methods

2.1. Construction of reporter plasmids and transient transfection

The 5′f region of the mPSP94 gene (GenBank AF087140) was cloned by precise PCR. Specific primers at positions −1202 and +21 from the transcription start site were designed (5′-AGCAACCTCACTTGTTCCTCAGA and 5′-GGTACCTCCAGCAAAGTCCTTG). PCR was performed with PrimStar Taq (Takara Bio., Otsu, Japan) and genomic DNA of C57BL mouse liver following the manufacturer's recommended conditions. After adding an adenosine residue, the PCR fragment was cloned into the pCR2.1-TOPO TA cloning vector (Invitrogen, Carlsbad, CA, U.S.A.) and the sequence confirmed with a capillary sequencer, ABI PRISM 310 (Applied Biosystems, Foster City, CA, U.S.A.). Truncated fragments of the 5′f region were also prepared by PCR with LA-Taq (Takara Bio.) between positions −450, −358, −200, −118, −95, −76 and +21 from the cloned 5′f region −1202/+21. Each fragment was cloned into the PCR2.1-TOPO vector. Sac I/Xho I-digested fragments were then inserted into the corresponding restriction enzyme sites of the pGL3-basic luciferase reporter plasmid (Promega, Madison, WI, U.S.A.), and designated as mPSP94p-1202, -450, -358, -200, -118, -95, -76.

Mutations and deletions were introduced into pGL3 promoters using a QuickChange Site-Directed Mutagenesis Kit (Agilent Technology, Santa Clara, CA, U.S.A.). For ARE analysis, nucleotides between positions −85 and −79, and between −44 and −31 were deleted from mPSP94p-118. In addition, the TGT sequence at position −84 was changed to GAG. For ERE analysis, estrogen responsive element (ERE)-like sequences between positions −435/−421 and −216/−202 were deleted from the PSP94p-450 reporter. Construction of the hAR and hER expression plasmids, pSG5-hAR, pSG5-hERα, pSG5-hERβ were as described previously [17]. PhRL-CMV (Promega) was utilized as an internal control.

CHO cells were plated at a concentration of 2×10^4/well in 48-well plates and transiently transfected with 300 ng of a reporter, 30 ng of pSG5-hAR and 2 ng of phRL-CMV with Hilymax transfection reagent containing a synthetic cationic lipid (Dojindo Laboratories, Kumamoto, Japan), following the manufacturer's protocol. The weight ratio of the reagent to DNA was 1:1. After 24 h of incubation, cells were harvested with 25 μl of cell lysis buffer (Promega) and firefly and renilla luciferase activities determined with a Dual Luciferase Assay Kit (Promega) by measuring luminescence with a Lumino/Fluro meter. Firefly luciferase reporter activity was normalized to renilla luciferase activity from phRL-CMV. For transfection into the LNCaP cell line, a concentration of 4×10^4 cells was plated into 48-well plates; the ratio of reagent to DNA was 3:1.

DNA motif searches for ARE and ERE were performed using TRANSFAC at http://www.genome.jp/tools/motif/.

2.2. Cell culture

The CHO cell line was maintained in DME medium (Sigma Chemical Co., St. Louis, Mo., U.S.A.) containing penicillin and streptomycin with 5% FBS (Biosolutions Japan Co., Osaka, Japan). The LNCaP cell line was maintained in RPMI-1640 medium (Sigma Chemical Co.) with 10% FBS and penicillin/streptomycin. For hormone treatment experiments, cells were maintained for a week in phenol red-free medium (Sigma Chemicals) containing the same antibiotics along with dextran-charcoal treated sera. Dihydrotestosterone (DHT), hydroxy flutamide (OH-flutamide), 17β-estradil (E_2) and ICI182780 were purchased from Wakojunyaku K.K., Osaka, Japan, Toronto Research Chemicals Inc., North York, ON, Canada, Sigma Chemicals and Tocris Bioscience, Ellisville, MI, U.S.A., respectively.

3. Results

3.1. DHT-dependent promoter activity of the 5′f region of mPSP94 gene

Data concerning promoter activity of the cloned 5′f region −1202/+21 and the successive truncated regions in response to DHT are summarized in Fig. 1A. Position numbers are assigned based upon the transcription start site (+1). Significant induction of luciferase activity by DHT was noted in all constructs but mPSP94p-76, which suggested that the region between positions −95 and −76 was essential for androgen-dependent transcription. The induction appeared lower with reporter constructs containing longer distal 5′f regions of the promoter, although these remained significant in terms of induction.

Since there is a half conserved ARE sequence between positions −84 and −79, luciferase activities of the mPSP94p-118 reporter deleting this region and a reporter exhibiting mutations within this site converting TGT to GAG at position −84 were examined and are shown in Fig. 1B. Those constructs disrupting the half ARE site showed no induction of luciferase activity in response to DHT, while a reporter constructing deleting elsewhere (Δ-44/-31) exhibited DHT-dependent transcription.

Induction of mPSP94p-118 reporter activity was DHT-dependent, and significant responses were identified with 10^{-11} M of DHT with maximal response at 10^{-9} M (Fig. 1C). An anti-androgen, OH-flutamide, antagonized the DHT-induced responses (Fig. 1D).

3.2. Enhancement of DHT responsive transcription in the presence of ERα

The observed increase in mPSP94-p1202 activity treated with DHT at 10^{-9} M was about 2.5 fold of the control, which was lower than that with mPSP94p-118. When an ERα expression vector was co-transfected in CHO cells along with the AR expression vector, the mPSP94p-1202 reporter activity in response to DHT increased significantly, but did not alter PSP94-p118-luc activity. Increased levels of ERα transfection resulted in higher PSP94-1202 activity in response to androgens (Fig. 2A). Transfection of ERβ, on the other hand, did not alter response to androgens. ICI 182780 suppressed the androgen-induced promoter activity of mPSP94 while E_2 administration did not alter activity (Fig. 2B).

3.3. ERE-like motifs in the 5′f region of mPSP94 gene

The enhancing effects of ERα were examined with successive truncated luciferase reporters (Fig. 3A). Significant enhancement was observed with PSP94p-1202 and -450 but not with -200 or -118. Since there are two ERE-like motifs at positions −435 and −216 in the promoter region, it is possible that these sequences may be involved in the ER-dependent enhancement of testosterone responses. When both ERE-like motifs were deleted in the PSP94p-450 reporter, the expected enhancement with ERα was lost, while deletions of only one of the EREs did not affect the enhancing effect (Fig. 3B).

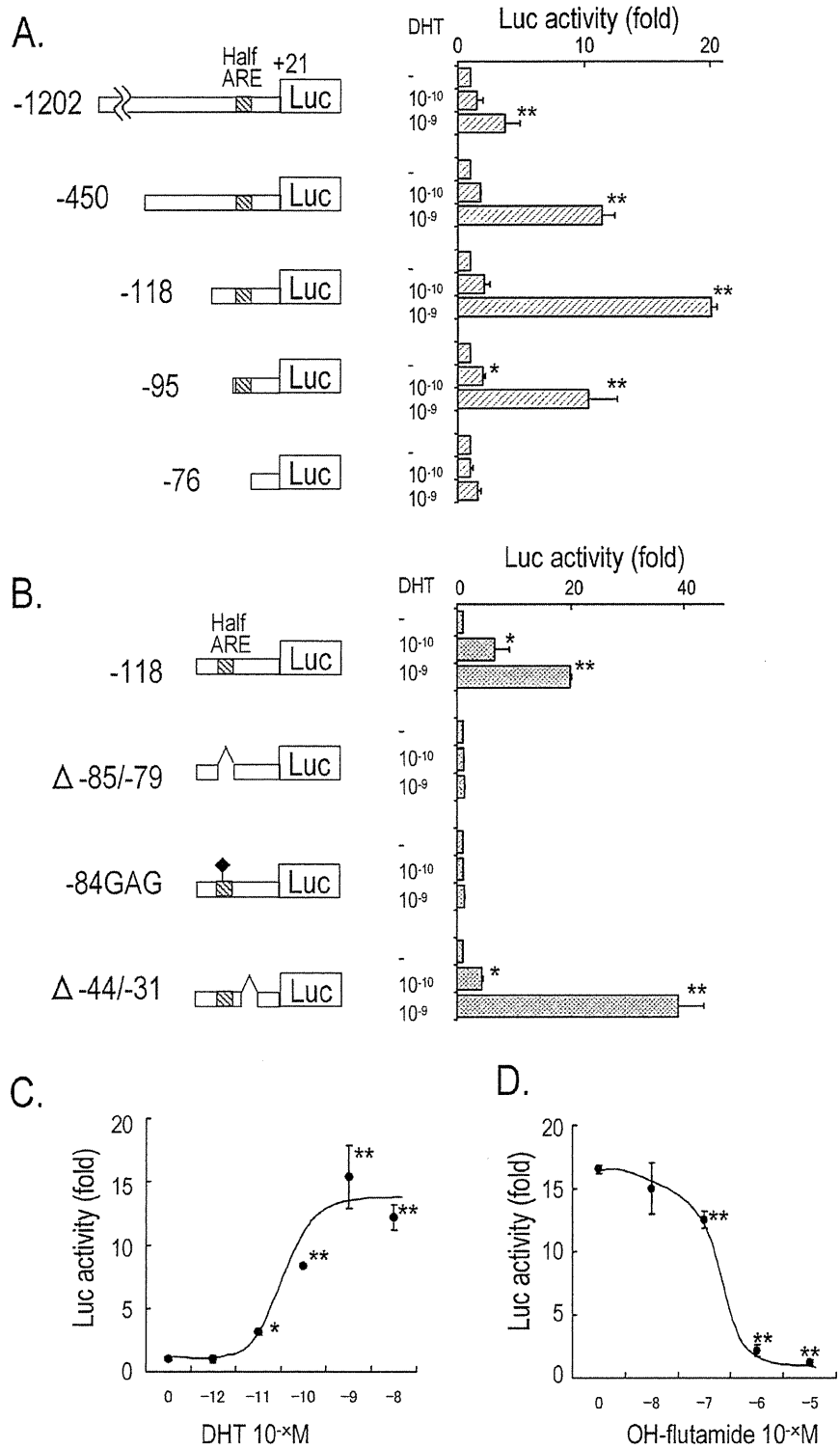

Fig. 1. DHT-dependent promoter activity of the mPSP94 gene in CHO cells. (A) Successive truncated fragments of the 5′f region from mPSP94 were inserted into a luciferase reporter. Position numbers were assigned based on the transcription start site (+1). Reporter plasmids (300 ng) and 30 ng of pSG5-hAR were transfected. DHT was administered at concentrations of 10^{-10} and 10^{-9} M. (B) DHT-induced luciferase activities of deletion and point mutants from the mPSP94p-118 reporter. (C) DHT-dose dependent induction of luciferase activity from the mPSP94p-118 reporter. (D) Dose dependent inhibition by OH-flutamide against DHT (10^{-9} M) induced activity. Bar indicates mean ± SEM, $n = 5$. *$p < 0.05$ and **$p < 0.01$ vs. control.

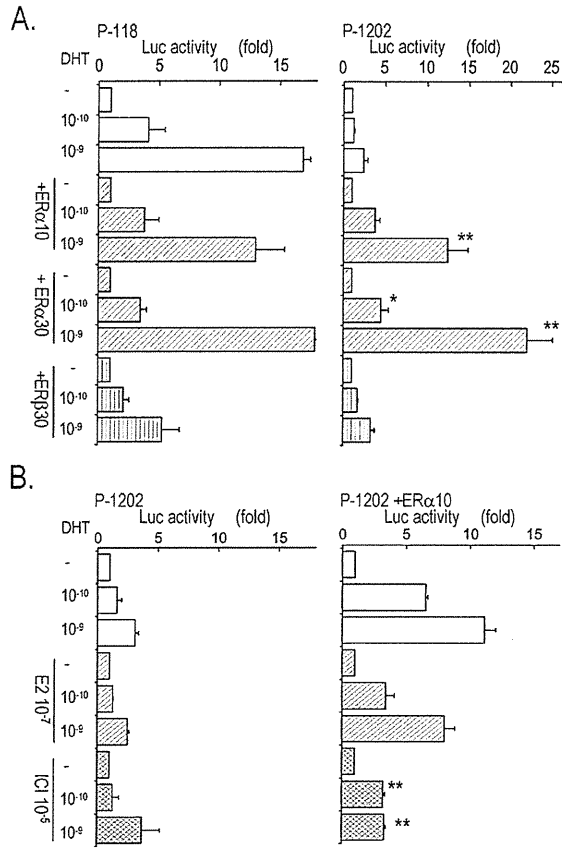

Fig. 2. Effects of ERα transfection upon DHT-dependent promoter activity of the mPSP94 gene in CHO cells. (A) Reporters containing p-118 or p-1202 were transfected along with 30 ng of pSG5-hAR and/or pSG5-hERα (10 or 30 ng) or pSG5-hERβ (30 ng). DHT was administered at concentrations of 10^{-10} or 10^{-9} M. (B) A reporter containing p-1202, pSG5-hAR and/or pSG5-hERα were transfected. DHT was administered at concentrations of 10^{-10} or 10^{-9} M with/without estradiol (E2) at 10^{-7} or ICI182178 at 10^{-5} M. Bar indicates mean ± SEM, $n = 5$. $^{*}p < 0.05$ and $^{**}p < 0.01$ vs. control.

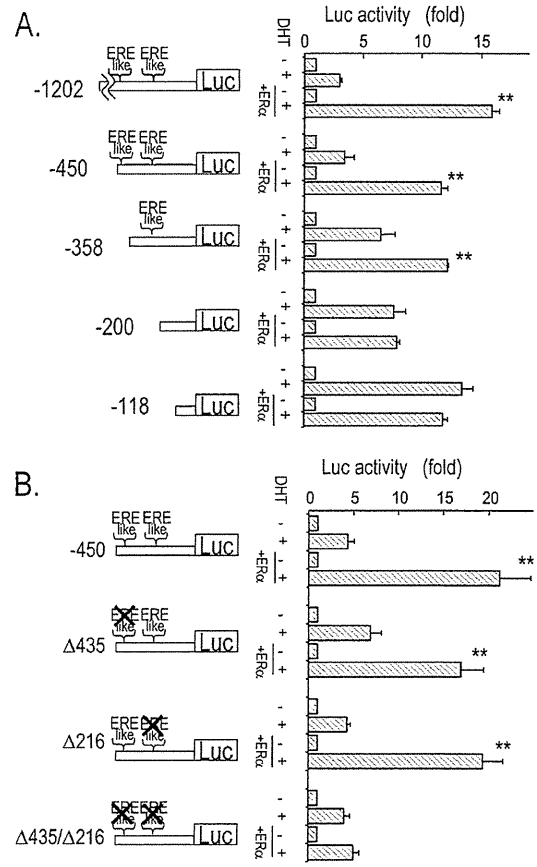

Fig. 3. Requirement of ERE-like motifs for ERα-dependent enhancing effects of androgen responses of the mPSP94 gene in CHO cells. (A) Successive truncated fragments of the mPSP94 promoter were transfected along with pSG5-hAR and pSG5-hERα. DHT was at 10^{-9} M. (B) Deletion mutants of pGL3-mPSP94p-450 were transfected with pSG5-hAR and pSG5-hERα. Bar indicates mean ± SEM, $n = 5$. $^{*}p < 0.05$ and $^{**}p < 0.01$ vs. ER negative control.

3.4. Promoter activity in LNCaP cells

Responses of reporter genes to DHT with successive truncated fragments of the mPSP94 promoter in the LNCaP cell line are summarized in Fig. 4A. Significant inductions were noted in all reporter constructs except mPSP94p-76. We also examined the effect of co-transfection with an ERα expression vector (Fig. 4B). With the mPSPp-118 reporter, ERα did not alter DHT responses, while mPSP94p-450 responses were significantly increased by co-transfection with the ERα expression vector. Co-transfection with the ERα expression vector did not change the response of mPSPp-450(Δ435/Δ216).

4. Discussion

PSP94 is a non-glycosylated and cysteine-rich protein composed of 94 amino acids [3,18,19]. First isolated from human seminal plasma, PSP94 was found to be one of the major prostatic proteins in humans [1]. Although the composition of rodent prostatic proteins is very different from that of humans, PSP94 is commonly expressed in rodents [5,20]. The function of this protein has yet to be fully determined. PSP94 exhibits immunoglobulin-binding capability in order to suppress the activation of B cells [7]. PSP94 may also function as an inhibitor of sperm motility [8].

Prostatic proteins are generally regulated by androgens. When the expression of proteins secreted from the mouse prostate was examined in our previous study, we found that all proteins were indeed significantly reduced just one week following castration of the animal but increased following androgen administration [21]. Some genes may be regulated by the direct interaction of liganded AR and promoter/enhancer regions of the gene, while other changes would be secondary or tertiary events along with involution and regeneration of the prostate tissue. In the case of PSP94, testosterone administration increased mRNA levels in castrated mice by a factor of 38 in just 24 h, suggesting that gene expression was directly controlled by androgens. PSP94 mRNA is expressed in ventral prostate as well as dorso-lateral prostate in the mouse, but is localized specifically in the dorso- and lateral-prostate lobes in the rat. In humans, the expression of PSP94 was not restricted to the prostate but was additionally detected in secretions from the respiratory tract, gastric fluid and other secretory tissues [18]. Since expression was very specific to the prostate in rodents, the promoter/enhancer structure of mPSP94 gene has drawn significant interest as potential gene targeting tools. It has been demonstrated that a 3.8 kb of the 5′f region was capable of directing gene expression in a prostate tissue specific mode, that was additionally ventral- and dorso-lateral lobe specific, in a transgenic mouse model [16].

Androgens regulate their responsive genes via intracellular ARs. Upon ligand binding, ARs interact with specific DNA sequences,

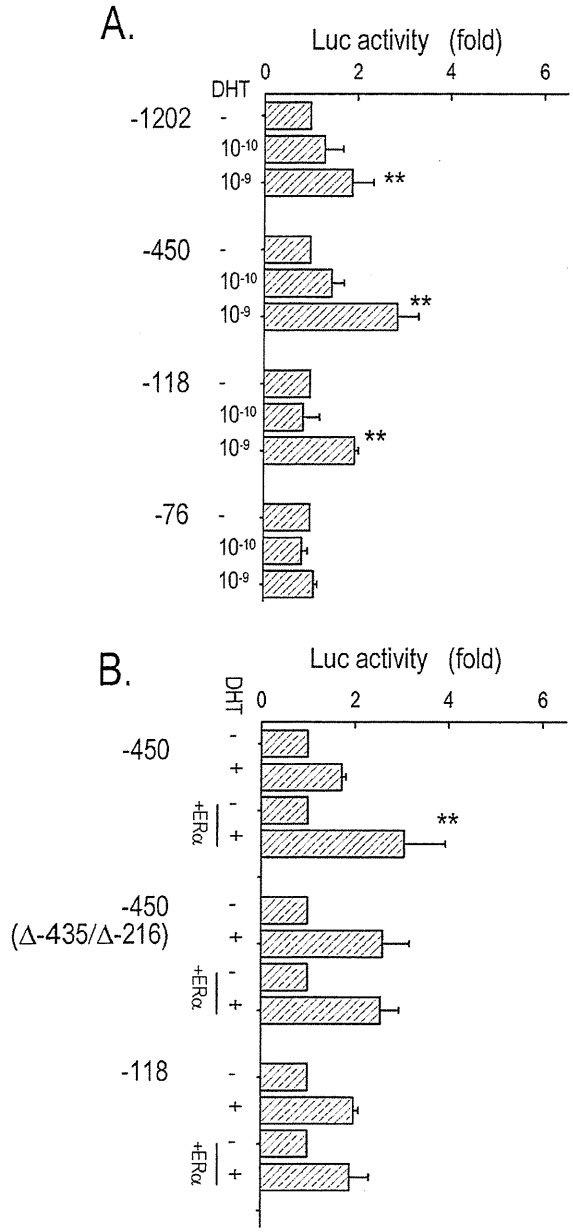

Fig. 4. DHT-dependent promoter activity of the mPSP94 gene in LNCaP cells. (A) Luciferase reporter constructs containing truncated fragments of the mPSP94 promoter were transfected and DHT was administered at concentrations of 10^{-10} and 10^{-9} M. (B) Reporter constructs containing p-450, ERE deleted p-450(Δ435/Δ 216) and p-118 were transfected with pSG5-hERα. DHT was at 10^{-9} M. Bar indicates mean ± SEM, $n = 5$. $^{**}p < 0.01$ vs. DHT negative control (A) and vs. ERα negative control (B).

known as AREs, and thus regulate the transcriptional activity of genes [22,23]. Steroid hormone receptors generally bind to DNA elements consisting of inverted repeats of six base pairs by three nucleotide spacers. The consensus hexametric sequence for AR is TGTTCT, which is identical to the glucocorticoid and progesterone responsive element. Previous investigations have revealed that AREs are divided into two categories; one interacts with glucocorticoids, mineralocorticoids and progesterone receptors, in addition to ARs, while the other is specific to ARs [24,25]. Previously described sequence data suggested that AR specific AREs tend to be organized as partial direct repeats rather than inverted repeats of the consensus hexametric repeat [22]. In mPSP94, we found an ARE candidate, TACCTAnnnTGTTCT that contains a half consensus ARE at position −93. Since androgen-dependent luciferase reporter activity was completely lost when this element was deleted or mutated, this motif between positions −93 and −79 appears to represent the functional ARE, although further studies are needed to determine if there are any direct interactions between this ARE-like sequence and AR. In the present study we primarily utilized CHO cells for the promoter assay since it is easy to perform transient transfection experiments in high efficiencies with this mammalian cell line. In addition, we used LNCaP, a human prostate adenocarcinoma cell line, to confirm the biological relevance of the promoter activity. LNCaP is an AR positive cell line that grows responding to testosterone and has been frequently used to study the androgen responsive gene regulation [26].

It has been demonstrated that combined administration of androgen and estrogen synergistically enhanced the development of prostatic hyperplasia and cancer in Noble rats as well as in chemical carcinogen-treated F344 rats [27,28]. In the previous study, we examined the expression of prostatic protein genes such as probasin and kallikrein S3 to understand the molecular mechanism underling the androgen plus estrogen effect [29]. We found that estradiol enhanced the androgen dependent expression of prostatic genes along with increase in ERα expression, which suggested that the elevated prostatic ERα may contribute to the enhancing effects. In the present study, we tested this hypothesis with PSP94 promoter and found that the androgen-dependent induction was enhanced by the presence of ERα while administration of estradiol did not change the transcription levels. In the PSP94 promoter, there are two ERE-like motifs that potentially interact with ERs at positions −435 and −216, ctannAnnnTGACCT and gGGnncnnnTGACCa, where the consensus ERE is ARGnnAnnnTGACCY. Results arising from deletion mutants indicated that at least one ERE similar motif is enough for the enhancement of androgen responses. These enhanced responses, however, did not exceed the degree of responses with the mPSP94p-118 reporter. Since reporters containing longer 5′f region displayed lower responses, it appears that the distal region of the promoter has suppressive function on the transcription and the presence of ERα may release the suppression. In normal adult prostate tissue, ERα expression is localized to stromal cells and ERβ is in epithelia [30]. In PC, however, epithelial expression of ERα increases while ERβ expression is reduced or lost [31–33]. During the development of PC, increasing ERα expression might enhance some critical androgen responsive genes related to prostatic carcinogenesis by the similar mechanisms found in the present study.

References

[1] P.A. Abrahamsson, H. Lilja, Three predominant prostatic proteins, Andrologia 22 (Suppl. 1) (1990) 122–131.
[2] J. Tremblay, G. Frenette, R.R. Tremblay, A. Dupont, M. Thabet, J.Y. Dube, Excretion of three major prostatic secretory proteins in the urine of normal men and patients with benign prostatic hypertrophy or prostate cancer, Prostate 10 (1987) 235–243.
[3] S. Garde, J.E. Fraser, N. Nematpoor, R. Pollex, C. Morin, A. Forte, S. Rabbani, C. Panchal, M.B. Gupta, Cloning expression, purification and functional characterization of recombinant human PSP94, Protein Expr. Purif. 54 (2007) 193–203.
[4] Y. Imasato, T. Onita, M. Moussa, H. Sakai, F.L. Chan, J. Koropatnick, J.L. Chin, J.W. Xuan, Rodent PSP94 gene expression is more specific to the dorsolateral prostate and less sensitive to androgen ablation than probasin, Endocrinology 142 (2001) 2138–2146.
[5] A. Thota, M. Karajgikar, W. Duan, M.Y. Gabril, F.L. Chan, Y.C. Wong, H. Sakai, J.L. Chin, M. Moussa, J.W. Xuan, Mouse PSP94 expression is prostate tissue-specific as demonstrated by a comparison of multiple antibodies against recombinant proteins, J. Cell Biochem. 88 (2003) 999–1011.
[6] M. Kamada, H. Mori, N. Maeda, S. Yamamoto, K. Kunimi, M. Takikawa, M. Maegawa, T. Aono, S. Futaki, S.S. Koide, beta-Microseminoprotein/prostatic secretory protein is a member of immunoglobulin binding factor family, Biochim. Biophys. Acta 1388 (1998) 101–110.

[7] A. Kumar, D.D. Jagtap, S.D. Mahale, M. Kumar, Crystal structure of prostate secretory protein PSP94 shows an edge-to-edge association of two monomers to form a homodimer, J. Mol. Biol. 397 (2010) 947–956.
[8] N. Aoki, A. Sakiyama, M. Deshimaru, S. Terada, Identification of novel serum proteins in a Japanese viper: homologs of mammalian PSP94, Biochem. Biophys. Res. Commun. 359 (2007) 330–334.
[9] R.J. Matusik, C. Kreis, P. McNicol, R. Sweetland, C. Mullin, W.H. Fleming, J.G. Dodd, Regulation of prostatic genes: role of androgens and zinc in gene expression, Biochem. Cell Biol. 64 (1986) 601–607.
[10] K.B. Cleutjens, C.C. van Eekelen, H.A. van der Korput, A.O. Brinkmann, J. Trapman, Two androgen response regions cooperate in steroid hormone regulated activity of the prostate-specific antigen promoter, J. Biol. Chem. 271 (1996) 6379–6388.
[11] Z. Wang, R. Tufts, R. Haleem, X. Cai, Genes regulated by androgen in the rat ventral prostate, Proc. Natl. Acad. Sci. U.S.A. 94 (1997) 12999–13004.
[12] P.H. Riegman, R.J. Vlietstra, J.A. van der Korput, A.O. Brinkmann, J. Trapman, The promoter of the prostate-specific antigen gene contains a functional androgen responsive element, Mol. Endocrinol. 5 (1991) 1921–1930.
[13] S. Zhang, P.E. Murtha, C.Y. Young, Defining a functional androgen responsive element in the 5′ far upstream flanking region of the prostate-specific antigen gene, Biochem. Biophys. Res. Commun. 231 (1997) 784–788.
[14] S. Kasper, P.S. Rennie, N. Bruchovsky, L. Lin, H. Cheng, R. Snoek, K. Dahlman-Wright, J.A. Gustafsson, R.P. Shiu, P.C. Sheppard, R.J. Matusik, Selective activation of the probasin androgen-responsive region by steroid hormones, J. Mol. Endocrinol. 22 (1999) 313–325.
[15] P.S. Rennie, N. Bruchovsky, K.J. Leco, P.C. Sheppard, S.A. McQueen, H. Cheng, R. Snoek, A. Hamel, M.E. Bock, B.S. MacDonald, Characterization of two cis-acting DNA elements involved in the androgen regulation of the probasin gene, Mol. Endocrinol. 7 (1993) 23–36.
[16] M.Y. Gabril, T. Onita, P.G. Ji, H. Sakai, F.L. Chan, J. Koropatnick, J.L. Chin, M. Moussa, J.W. Xuan, Prostate targeting: PSP94 gene promoter/enhancer region directed prostate tissue-specific expression in a transgenic mouse prostate cancer model, Gene Ther. 9 (2002) 1589–1599.
[17] S. Kitamura, T. Suzuki, S. Ohta, N. Fujimoto, Antiandrogenic activity and metabolism of the organophosphorus pesticide fenthion and related compounds, Environ. Health Perspect. 111 (2003) 503–508.
[18] J.W. Xuan, D. Wu, Y. Guo, S. Garde, D.T. Shum, M. Mbikay, R. Zhong, J.L. Chin, Molecular cloning and gene expression analysis of PSP94 (prostate secretory protein of 94 amino acids) in primates, DNA Cell Biol. 16 (1997) 627–638.
[19] J.W. Xuan, J. Kwong, F.L. Chan, M. Ricci, Y. Imasato, H. Sakai, G.H. Fong, C. Panchal, J.L Chin, cDNA, genomic cloning, and gene expression analysis of mouse PSP94 (prostate secretory protein of 94 amino acids), DNA Cell Biol. 18 (1999) 11–26.
[20] J. Kwong, J.W. Xuan, H.L. Choi, P.S. Chan, F.L. Chan, PSP94 (or beta-microseminoprotein) is a secretory protein specifically expressed and synthesized in the lateral lobe of the rat prostate, Prostate 42 (2000) 219–229.
[21] N. Fujimoto, Y. Akimoto, T. Suzuki, S. Kitamura, S. Ohta, Identification of prostatic-secreted proteins in mice by mass spectrometric analysis and evaluation of lobe-specific and androgen-dependent mRNA expression, J. Endocrinol. 190 (2006) 793–803.
[22] F. Claessens, S. Denayer, N. Van Tilborgh, S. Kerkhofs, C. Helsen, A. Haelens, Diverse roles of androgen receptor (AR) domains in AR-mediated signaling, Nucl. Recept. Signal. 6 (2008) e008.
[23] E.C. Bolton, A.Y. So, C. Chaivorapol, C.M. Haqq, H. Li, K.R. Yamamoto, Cell- and gene-specific regulation of primary target genes by the androgen receptor, Genes Dev. 21 (2007) 2005–2017.
[24] P.S. Nelson, N. Clegg, H. Arnold, C. Ferguson, M. Bonham, J. White, L. Hood, B. Lin, The program of androgen-responsive genes in neoplastic prostate epithelium, Proc. Natl. Acad. Sci. U.S.A. 99 (2002) 11890–11895.
[25] F. Claessens, G. Verrijdt, E. Schoenmakers, A. Haelens, B. Peeters, G. Verhoeven, W. Rombauts, Selective DNA binding by the androgen receptor as a mechanism for hormone-specific gene regulation, J. Steroid Biochem. Mol. Biol. 76 (2001) 23–30.
[26] J. Veldscholte, C.A. Berrevoets, E. Mulder, Studies on the human prostatic cancer cell line LNCaP, J. Steroid Biochem. Mol. Biol. 49 (1994) 341–346.
[27] R.L. Noble, The development of prostatic adenocarcinoma in Nb rats following prolonged sex hormone administration, Cancer Res. 37 (1977) 1929–1933.
[28] K. Suzuki, Y. Takezawa, T. Suzuki, S. Honma, H. Yamanaka, Synergistic effects of estrogen with androgen on the prostate—effects of estrogen on the prostate of androgen-administered rats and 5-alpha-reductase activity, Prostate 25 (1994) 169–176.
[29] N. Fujimoto, H. Honda, T. Suzuki, S. Kitamura, Estrogen enhancement of androgen-responsive gene expression in hormone-induced hyperplasia in the ventral prostate of F344 rats, Cancer Sci. 95 (2004) 711–715.
[30] T. Tsurusaki, D. Aoki, H. Kanetake, S. Inoue, M. Muramatsu, Y. Hishikawa, T. Koji, Zone-dependent expression of estrogen receptors alpha and beta in human benign prostatic hyperplasia, J. Clin. Endocrinol. Metab. 88 (2003) 1333–1340.
[31] G.S. Yang, Y. Wang, P. Wang, Z.D. Chen, Expression of oestrogen receptor-alpha and oestrogen receptor-beta in prostate cancer, Chin. Med. J. (Engl.) 120 (2007) 1611–1615.
[32] M. Royuela, M.P. de Miguel, F.R. Bethencourt, M. Sanchez-Chapado, B. Fraile, M.I. Arenas, R. Paniagua, Estrogen receptors alpha and beta in the normal, hyperplastic and carcinomatous human prostate, J. Endocrinol. 168 (2001) 447–454.
[33] L.G. Horvath, S.M. Henshall, C.S. Lee, D.R. Head, D.I. Quinn, S. Makela, W. Delprado, D. Golovsky, P.C. Brenner, G. O'Neill, R. Kooner, P.D. Stricker, J.J. Grygiel, J.A. Gustafsson, R.L. Sutherland, Frequent loss of estrogen receptor-beta expression in prostate cancer, Cancer Res. 61 (2001) 5331–5335.

J Occup Health 2011; 53: 51–63

Journal of Occupational Health

Two- and 13-week Inhalation Toxicities of Indium-tin Oxide and Indium Oxide in Rats

Kasuke NAGANO[1], Kaoru GOTOH[1], Tatsuya KASAI[1], Shigetoshi AISO[1], Tomoshi NISHIZAWA[1], Makoto OHNISHI[1], Naoki IKAWA[1], Yoko EITAKI[2], Kenichi YAMADA[2], Heihachiro ARITO[1] and Shoji FUKUSHIMA[1]

[1]Japan Bioassay Research Center, Japan Industrial Safety and Health Association and [2]Occupational Health Research and Development Center, Japan Industrial Safety and Health Association, Japan

Abstract: Two- and 13-week Inhalation Toxicities of Indium-tin Oxide and Indium Oxide in Rats: Kasuke NAGANO, *et al.* Japan Bioassay Research Center, Japan Industrial Safety and Health Association—Objectives: Two- and 13-week inhalation toxicities of indium-tin oxide (ITO) and indium oxide (IO) were characterized for risk assessments of workers exposed to ITO. **Methods:** F344 rats of both sexes were exposed by inhalation to ITO or IO aerosol for 6 h/day, 5 day/wk for 2 wk at 0, 0.1, 1, 10 or 100 mg/m^3 or 13 wk at 0, 0.1or 1 mg/m^3. An aerosol generator and inhalation exposure system was constructed. **Results:** Blood and lung contents of indium were elevated in a dose-related manner in the ITO- and IO-exposed rats. ITO and IO particles were deposited in the lung, mediastinal lymph node and nasal-associated lymphoid tissue. Exposures to ITO and IO induced alveolar proteinosis, infiltrations of alveolar macrophages and inflammatory cells and alveolar epithelial hyperplasia in addition to increased lung weight. ITO affected the lung more severely than IO did. Fibrosis of alveolar wall developed and some of these lesions worsened at the end of the 26-week post-exposure period. **Conclusions:** Persistent pulmonary lesions including alveolar proteinosis and macrophage infiltration occurred after 2- and 13-week inhalation exposures of rats to ITO and IO. Fibrosis of alveolar wall developed later. These lesions occurred after ITO exposure at the same concentration as the current occupational exposure limit in the USA and at blood indium levels below the biological exposure index in Japan for indium.
(J Occup Health 2011; 53: 51–63)

Received Sep 17, 2010; Accepted Nov 15, 2010
Published online in J-STAGE Jan 11, 2011
Correspondence to: T. Nishizawa, Japan Bioassay Research Center, Japan Industrial Safety and Health Association, 2445 Hirasawa, Hadano, Kanagawa 257-0015, Japan
(e-mail: t-nishizawa@jisha.or.jp)

Key words: Indium-tin oxide, Indium oxide, Inhalation, Pulmonary toxicity, Rat

Indium-tin oxide (ITO), a sintered material containing 90% indium oxide (IO) and 10% tin oxide, has been extensively used in liquid-crystal displays and other display devices. The average annual growth of the use of indium in the form of ITO has increased by an average 18 percent per year[1]. The technology used to create ITO targets and ITO thin film applications gives rise to potential exposure to ITO particles, and poses a serious threat to the health of workers engaged in the manufacturing, processing and handling of ITO. Two fatal case studies have been reported. An operator of wet surface grinding in an ITO plant was diagnosed as interstitial pneumonia and died of bilateral pneumothorax[2], and a furnace operator in an ITO plant died of respiratory failure due to pulmonary alveolar proteinosis[3]. Recent epidemiological studies on the health of workers in ITO plants have demonstrated a potential cause of occupational lung disease as inhaled indium and an increased risk for interstitial lung damage by ITO inhalation[4–7]. Experimental toxicology studies have revealed that an administration of ITO causes persistent inflammation in the lung of rats[8], a strong cytotoxic response of macrophages *in vitro* by generation of reactive oxygen species (ROS)[8], and a pulmonary inflammatory response with diffuse bronchiolar and alveolar hyperplasia and interstitial fibrotic proliferation in hamsters[9,10]. An intratracheal administration of indium trichloride to rats was reported to initiate an inflammatory response with rapid development of fibrosis[11]. The National Toxicology Program's (NTP's) 14-week study[12] showed that inhalation exposure of rats to indium phosphide aerosol induces inflammation and alveolar proteinosis in the lung.

Inhalation is a principal route of exposure for workers in the facilities where ITO is manufactured, processed and

handled. In order to protect workers from inhalation exposure to indium and its compounds, an occupational exposure limit (OEL) of 0.1 mg/m^3 has been recommended as the Threshold Limit Value-Time Weighted Average (TLV-TWA) by the American Conference of Governmental Industrial Hygienists (ACGIH)[13], and as the Recommended Exposure Limit (REL) by the National Institute for Occupational Safety and Health (NIOSH)[14]. The Japan Society for Occupational Health (JSOH)[15] has recommended a serum indium level of 3 μg/l as a biological exposure index (BEI). It is of prime importance to provide basic animal toxicity data showing the dose-response relationships between concentrations of inhalation exposure of rats and mice to ITO and its major component, IO, target tissue doses of indium and resulting pulmonary toxic responses to these two aerosols.

In order to assess the health risks of workers exposed by inhalation to ITO and IO aerosols in the work environment, the present studies were intended to characterize subacute and subchronic inhalation toxicities of ITO and IO in rats and to provide dose-response relationships between aerosol concentrations of inhalation exposure to ITO and IO aerosols, lung and blood contents of indium and resulting pulmonary lesions. For this purpose, we constructed an aerosol generation and exposure system for providing inhalation exposure of unrestrained rats and mice to aerosols of ITO and IO at strictly controlled exposure concentrations ranging from 0.1 to 100 mg/m^3. And, we conducted inhalation exposures of male and female rats to dry aerosols of ITO and IO at these concentrations for 2 and 13 wk. A further purpose of the present studies was to predict an appropriate range of exposure concentrations of ITO aerosol for a 2-year rodent carcinogenicity study, based on the results.

Materials and Methods

The present studies were conducted in accordance with the Organization for Economic Cooperation and Development's (OECD's) Good Laboratory Practice[16], and with reference to the OECD's Guidelines for Testing of Chemicals 412 "Repeated Dose Inhalation Toxicity, 28-day or 14-day Study"[17] and 413 "Subchronic Inhalation Toxicity, 90-day Study"[18]. The animals were cared for in accordance with the Guide for the Care and Use of Laboratory Animals[19] and the present studies were approved by the ethics committee of the Japan Bioassay Research Center.

Test materials

Powders of ITO and IO were kindly supplied by JX Nippon Mining & Metals, Corp. (former Nippon Mining & Metals Co., Ltd.) (Tokyo, Japan). ITO powder was prepared by grinding the sintered ITO plate, and was colored with black. The mean diameter of the powder was 3.5 μm with a 90% cumulative diameter of 8.9 μm. The sintered ITO powder was composed of 90.06% IO and 9.74% SnO_2. Its purity was 99.8% with trace amounts of aluminium, chromium, copper, iron, nickel, lead, silica, zirconium and zinc as impurities. IO powder was colored with yellow, and had a mean diameter of 1.4 μm with a 90% cumulative diameter of 2.9 μm. The purity of the IO powder was 99.9% with trace amounts of tin, silica and lead as impurities.

Animals

F344/DuCrlCrlj rats of both sexes were obtained at the age of 4 wk from Charles River Japan, Inc (Kanagawa, Japan). The animals were quarantined and acclimated for 2 wk before the start of experiment. The animals were housed individually in stainless-steel wire hanging cages (170 W × 294 D × 176 H mm), which were placed in a stainless steel inhalation exposure chamber of 1,060 liters in volume. The environment in the exposure chamber was maintained constant at a temperature of 20–24°C and a relative humidity of 30–70% with 12 air changes/h. The exposure chambers were installed in a barrier system animal room. Fluorescent lighting was controlled automatically to give a 12-hour light/dark cycle. All rats were given sterilized commercial pellet diet (CRF-1, Oriental Yeast Co., Ltd., Tokyo, Japan) and sterilized water *ad libitum*.

Experimental design

In the 2-week study, groups of 5 rats of each sex were exposed to ITO or IO aerosol at a target concentration of 0.1, 1, 10 or 100 mg/m^3 as ITO or IO for 6 h/day, 5 day/wk for 2 wk. In the 13-week study, groups of 10 rats of each sex were exposed to ITO or IO aerosol at a target concentration of 0.1 or 1 mg/m^3 for 6 h/day, 5 day/wk for 13 wk. Groups of 5 or 10 rats of each sex were exposed to clean air for 2 or 13 wk under the same conditions, and served as respective controls. In order to evaluate recovery from the subchronic effects after cessation of the 13-week exposure to ITO, a post-exposure group of 10 rats of each sex was set up, which was exposed to ITO at 0.1 mg/m^3 for 13 wk and then to clean air for 26 wk. Ten rats of each sex serving as respective controls were handled in the same manner as the post-exposure group, but were exposed to clean air for 39 wk.

Aerosol generation and exposure to ITO and IO

Two different systems for generation of ITO or IO aerosol and inhalation exposure were used in the present studies. A target aerosol concentration of 100 mg/m^3 was generated using a system illustrated in the upper part (A) of Fig. 1. It consisted of a dust feeder equipped with an ejector, an exposure chamber and a digital dust indicator (Type AP-632T, Sibata Scientific Technology, Ltd., Tokyo, Japan). Airflow containing the aerosol was generated by drawing the powder with compressed clean air at the first

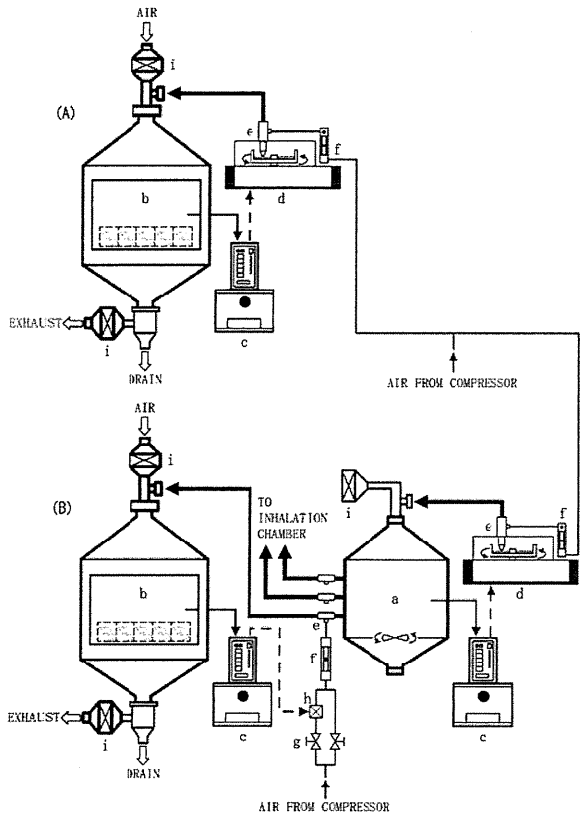

Fig. 1. A schematic diagram of the aerosol generation, regulation and inhalation exposure systems. (A) A system used for aerosol generation of a high aerosol concentration of 100 mg/m³. (B) Another system used for generation of lower concentrations of 10, 1 and 0.1 mg/m³. Thick, thin and dotted arrows indicate aerosol flow, sampling of chamber air for monitoring aerosol concentration and feedback control, respectively. Components of the systems: a) reservoir chamber, b) inhalation exposure chamber, c) digital dust indicator, d) dust feeder with an ejector, e) ejector, f) flowmeter, g) flow control valve, h) solenoid valve, i) HEPA filter.

ejector and introduced into the top of the exposure chamber where the filtered air had been kept flowing downward at 12 air changes/h. The mass-equivalent concentration of ITO or IO in the exposure chamber was monitored with the digital dust indicator. In order to keep the aerosol concentration constant in the exposure chamber during the 6-hour exposure period, a feedback control system between the digital dust indicator and the dust feeder was set up. When the chamber concentration went above an upper limit of a normal concentration range, the dust feeder stopped supplying the powder. Conversely, when the chamber concentration fell below the lower limit, the dust feeder started to supply the powder. Chamber concentrations of 10, 1 and 0.1 mg/m³ were generated using another system illustrated in the lower part (B) of Fig. 1. It consisted of the first-stage system (a, c and d in Fig. 1B) for aerosol generation of a high concentration at 100 mg/m³ and a further dilution system. Aerosol generation of the high concentration and its regulation were performed in the same manner described above, and airflow containing the aerosol was delivered to a reservoir chamber for stabilization of the aerosol concentration. The airflow containing the aerosol was delivered to the second ejector and then introduced into the top of the exposure chambers where the filtered air had been kept flowing downward at 12 air changes/h. The aerosol concentration in the exposure chamber was monitored with the second digital dust indicator and regulated at a target concentration of 10, 1 or 0.1 mg/m³. The aerosol concentration was stabilized by setting up the second feedback system between the digital dust indicator and a solenoid valve which regulated the flow rate of compressed clean air entering the second ejectors. The exposure chambers were kept at a negative pressure (–100 Pa), in order to prevent leakage of ITO and IO aerosols into the outside air. Exhaust air from the exposure chamber was passed through a HEPA filter to remove ITO and IO particles before release into the atmosphere. The concentrations of indium in the exhaust air were below the detection limit of 0.0001 mg/m³ after the treatment with the HEPA filter.

Chamber concentrations and size distribution of ITO and IO aerosols

In order to determine concentrations of ITO or IO aerosol in the exposure chamber, ITO or IO particles were collected on a filter (Teflon binder T60A20, Sibata Scientific Technology, Ltd, Tokyo, Japan) on Days 1 and 8 in the 2-week study and every week in the 13-week study. The particles on the filter were dissolved in a mixture solution of distilled water, hydrochloric acid and nitric acid (2:2:1 by volume ratio) at 160°C. The resulting solution was diluted with nitric acid, and then subjected to atomic absorption spectrometry analysis (Polarized Zeeman Atomic Absorption Spectrophotometer, Z-5010, Hitachi High-Technol. Co., Tokyo, Japan). Exposure chamber concentrations of ITO and IO aerosols were derived from the measured levels of elemental indium as shown in Table 1.

Measurement of the size distribution of ITO or IO aerosol in the exposure chamber was carried out once in the 2-week study and in the 4th and 8th wk in the 13-week study. ITO or IO aerosol was collected with an 8-stage Andersen sampler (Type AN200, Sibata Scientific Technology, Ltd). Using the mass of the particles on the filter (Teflon binder T60A20, Sibata Scientific Technology, Ltd) collected at each stage of the Andersen sampler, mass median aerodynamic diameter (MMAD) and geometric standard deviation (GSD) were determined.

Table 1. Mass concentrations and mass median aerodynamic diameters (MMADs) and geometric standard deviations (GSDs) of ITO and IO aerosols in the exposure chamber

	ITO				IO			
	Mass concentration (mg/m^3)		Aerodynamic diameter		Mass concentration (mg/m^3)		Aerodynamic diameter	
Dose	(Mean ± SD)		Median (μm)	GSD	(Mean ± SD)		Median (μm)	GSD
2-week study		In a)				In a)		
0.1 mg/m^3	0.09 ± 0.00	0.07 ± 0.00	2.5	1.8	0.10 ± 0.01	0.08 ± 0.01	1.9	1.7
1 mg/m^3	0.94 ± 0.02	0.70 ± 0.01	2.7	1.8	1.07 ± 0.06	0.89 ± 0.05	2.1	1.8
10 mg/m^3	9.33 ± 0.33	6.94 ± 0.25	3.0	1.8	10.76 ± 0.46	8.90 ± 0.38	2.1	1.8
100 mg/m^3	95.90 ± 2.99	71.35 ± 2.22	3.7	1.9	105.25 ± 7.01	87.04 ± 5.80	2.2	1.7
13-week study								
0.1 mg/m^3	0.10 ± 0.01	0.07 ± 0.01	2.4	1.8	0.10 ± 0.01	0.08 ± 0.01	2.1	1.7
1 mg/m^3	1.01 ± 0.08	0.75 ± 0.06	2.5	1.9	1.01 ± 0.09	0.84 ± 0.07	2.3	1.7

a): Mass concentration as indium.

Determination of indium concentrations in the lung and blood

Lung indium was quantified in the 2-week study, and both the lung and whole-blood were analyzed for indium in the 13-week study. Cranial, caudal and accessory lobes of the right lung were used for the analysis. A sample of the lung or 1.0 m*l* of blood was added with ultra-pure nitric acid and digested with a microwave digestion apparatus (Microwave Digestion System, Model 7295, O·I·Analytical, CA, USA). The digested sample was added with ultra-pure water and injected into an inductively coupled plasma mass spectrometer (ICP-MS) (Type 7500i, Agilent Technologies, Ltd., CA, USA). Cesium was used as an internal standard for the indium measurement. The quantitative detection limit of indium was 0.006 $\mu g/g$ for lung tissue and 0.5 $\mu g/l$ for whole-blood. Lung indium was expressed as both a concentration of indium per gram of lung tissue and the content of indium in the whole-lung.

Clinical observations and pathological examinations

The animals were observed daily for their clinical signs and mortality. Body weight and food consumption were measured weekly throughout the study periods. Animals surviving to the end of the 2- or 13-week exposure period and to the end of the 26-week post-exposure period received complete necropsy. Blood was collected for blood indium, hematology and blood biochemistry from the abdominal aorta under etherization. The organs and tissues designated in the OECD test guidelines[17, 18] were examined macroscopically and microscopically. The tissues were fixed in 10% neutral buffered formalin, and embedded in paraffin. Tissue sections of 5 μm in thickness were prepared, and stained with hematoxylin and eosin (H & E). The sections of lung tissue were also stained with a periodic acid Schiff (PAS) reagent. Lesions of the lung and lymph nodes were evaluated for their severities, scoring on a scale of "slight" to "severe" with reference to the criteria of non-neoplastic lesions by Shackelford *et al.*[20].

Statistical analysis

Body weight, organ weight, and hematological and blood biochemical parameters were analyzed by Dunnett's test as described previously[21]. Histopathological findings in the 13-week study were analyzed by chi-square test. A two-tailed test was used for all statistics. In all cases, a p value of 0.05 was used as the level of significance.

Results

Exposure chamber concentrations and size distributions of ITO and IO aerosol

Table 1 shows the mass concentrations derived from the measured levels of elemental indium (mean ± SD), MMADs and GSDs of ITO and IO aerosols in the exposure chamber. The exposure concentrations of ITO and IO aerosols were found to be regulated precisely within less than 10% in the variation coefficient and accurately within less than 10% deviation from the target concentrations. MMADs of the ITO aerosol tended to slightly increase with an increase in the chamber concentrations, while the GSDs were constant at all exposure concentrations. On the other hand, MMADs and GSDs of IO aerosol were constant over a wide range of exposure concentrations, and MMADs of IO aerosol were slightly smaller than those of ITO aerosol.

Indium concentrations in the lung and blood

Table 2 shows lung and blood contents of indium in the male and female rats exposed to ITO and IO for 2 and 13 wk. Lung contents of indium expressed as $\mu g/g$ lung tissue and μg/whole-lung were increased with an increase in the concentration of exposure to ITO or IO, but the exposure concentration-related increase was smaller in the unit of $\mu g/g$ lung tissue than in that of μg/whole-lung, because the lung weights of the exposed rats were significantly heavier, up to 2-fold heavier than those of the control groups, depending on the exposure concentration (Fig. 2). In the 2-week study, the whole-lung contents of indium in the

Table 2. Lung and blood contents of indium in the male and female rats exposed to ITO or IO at 4 different concentrations for 2 wk, in those exposed to ITO or IO at 0.1 or 1 mg/m³ for 13 wk, and in those exposed to ITO at 0.1 mg/m³ for 13 wk followed by exposure to clean air for 26 wk

	2-week study				13-week study		
Group name (mg/m³)	0.1	1	10	100	0.1	0.1 (P)	1
No. of animals examined	5	5	5	5	10	10	10
<ITO>							
Male							
Lung (μg/g as In)	3.3 ± 0.3	32.4 ± 2.7	127.6 ± 17.7	470.3 ± 58.1	24.0 ± 2.7	8.8 ± 1.1	74.4 ± 10.5
Lung (μg/whole-lung as In)	2.4 ± 0.1	31.1 ± 1.8	165.1 ± 9.8	688.3 ± 43.1	38.7 ± 4.6	15.0 ± 2.0	173.9 ± 28.6
Blood (μg/l as In)	–	–	–	–	0.77 ± 0.09	1.04 ± 0.10	3.39 ± 0.33
Female							
Lung (μg/g as In)	2.9 ± 0.4	34.8 ± 8.8	148.0 ± 41.2	533.9 ± 69.1	22.9 ± 2.2	8.6 ± 1.0	79.9 ± 7.1
Lung (μg/whole-lung as In)	1.8 ± 0.2	28.1 ± 7.2	157.4 ± 41.9	658.7 ± 70.9	26.3 ± 2.7	10.3 ± 1.1	134.6 ± 8.0
Blood (μg/l as In)	–	–	–	–	1.13 ± 0.32	1.46 ± 0.26	4.06 ± 0.56
<IO>							
Male							
Lung (μg/g as In)	5.3 ± 0.5	61.3 ± 11.1	261.7 ± 7.2	1124.7 ± 49.3	18.0 ± 2.3	–	144.2 ± 15.7
Lung (μg/whole-lung as In)	3.7 ± 0.3	45.1 ± 5.7	324.5 ± 20.0	1689.2 ± 64.2	17.2 ± 2.8	–	235.5 ± 34.0
Blood (μg/l as In)	–	–	–	–	ND	–	0.76 ± 0.08
Female							
Lung (μg/g as In)	5.0 ± 0.3	52.8 ± 3.2	267.0 ± 25.5	1190.8 ± 51.0	13.4 ± 1.5	–	130.6 ± 15.7
Lung (μg/whole-lung as In)	3.1 ± 0.2	33.8 ± 3.2	263.8 ± 26.7	1464.1 ± 88.2	9.8 ± 1.0	–	157.3 ± 17.4
Blood (μg/l as In)	–	–	–	–	ND	–	0.96 ± 0.26

(P): Data at the end of the 26-week post-exposure period. Values indicate mean ± SD. ND: Contents were below the quantitative detection limit (0.5 μg/l). –: Not examined.

ITO- and IO-exposed groups of both sexes were not increased in a manner proportional to the exposure concentration. The whole-lung contents of indium were lower in the ITO-exposed groups than in the IO-exposed groups of both sexes at all exposure concentrations. In the 13-week study, the exposure concentration-related increase in the whole-lung content of indium was also disproportionately lowered to greater extent in the ITO-exposed rats than in the IO-exposed rats. Unlike the result from the 2-week study, the whole-lung contents of indium in the 0.1 mg/m³ ITO-exposed rats of both sexes were higher than those of the 0.1 mg/m³ IO-exposed rats of both sexes. The whole-lung contents of indium in the ITO-exposed rats of both sexes measured at the end of the 26-week post-exposure period were lowered to 40% as compared with those measured at the end of the 13-week exposure.

Table 2 also shows the blood contents of indium in the male and female rats at the end of 13-week exposures to ITO and IO at 0.1 and 1 mg/m³ as well as those exposed to ITO at 0.1 mg/m³ for 13 wk and then to clean air for 26 wk. The blood contents of indium in the 0.1 mg/m³ IO-exposed rats of both sexes were below the quantitative detection limit of 0.5 μg/l. The blood contents of indium in the 1 mg/m³ ITO-exposed groups of both sexes were 4-fold higher than those in 1 mg/m³ IO-exposed group of both sexes. The blood contents of indium in the 0.1 mg/m³ ITO-exposed rats of both sexes measured at the end of the 26-week post-exposure period were 1.3-fold higher than those measured at the end of the 13-week exposure period.

Mortality and clinical signs in the 2- and 13-week studies

Neither death nor abnormal clinical sign, such as irregular sounds of respiration, was observed in any group exposed to ITO or IO for 2 or 13 wk. There was no growth retardation in any group exposed to ITO or IO for 2 or 13 wk as compared with the growth rate in the respective control.

Hematological and blood biochemical changes in the 2- and 13-week studies

In the 2-week study, white blood cell counts in the 100

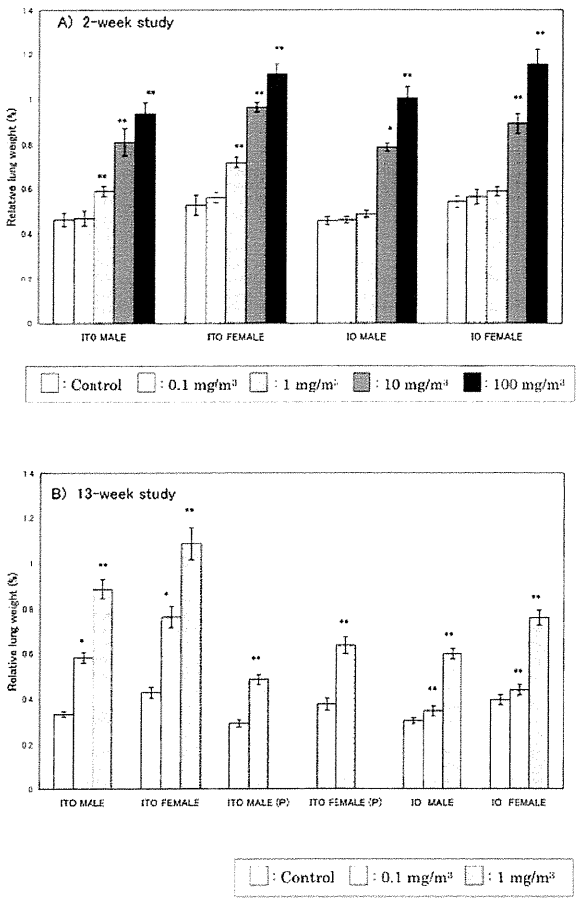

Fig. 2. Relative lung weights: A) in the rats of both sexes exposed to ITO or IO aerosol at 0, 0.1, 1, 10 or 100 mg/m³ for 2 wk, B) in the rats of both sexes exposed to ITO or IO aerosol at 0, 0.1 or 1 mg/m³ for 13 wk. (P) represents the rats of both sexes exposed to ITO aerosol at 0 or 0.1 mg/m³ for 13 wk and subsequently to clean air for 26 wk.

mg/m³ ITO-exposed male rats and red blood cell counts, hemoglobin and hematocrit values in the 100 mg/m³ IO-exposed male rats were significantly increased compared with the respective control groups. In the 13-week study, potassium was significantly decreased in both 0.1 and 1 mg/m³ ITO- and IO-exposed rats. In addition, significant decreases in sodium and chlorine in the 0.1 and 1 mg/m³ IO-exposed male rats and significantly decreased triglyceride in the 0.1 and 1 mg/m³ IO-exposed female rats were also observed (data not shown).

Pathological findings in the 2-week study

Relative lung weights were significantly increased in the male and female rats exposed to ITO at 1 mg/m³ and above compared with the respective control groups, whereas significantly increased lung weights were noted in the rats of both sexes exposed to IO only at 10 and 100 mg/m³ compared with the respective control groups (Fig. 2-A). Increases in absolute lung weights were indicated as well (data not shown).

Microscopic examination revealed that ITO and IO particles were deposited in the lungs of all the exposed rats except those exposed to the 0.1 mg/m³ (Table 3). The particles were pale brown and transparent, looked like amber, and were located primarily within the alveolar macrophages (Fig. 3-1) and partly as a free form in the alveolar space. Both ITO and IO particles were deposited separately as single particles. ITO and IO particles were also observed to lesser extent in the bronchus-associated lymphoid tissue (BALT) of the lung, in the mediastinal lymph nodes (MLN) and in the nasal-associated lymphoid tissue (NALT) of the nasopharyngeal duct. The particles were located within macrophages, and notably, degenerative alveolar macrophages engulfing the particles were often observed (Fig. 3-1). The most remarkable lesion found in the present 2-week study was alveolar proteinosis characterized by filling of the alveolar space with a granular, pale eosinophilic material in the ITO- and IO-exposed rats. The diagnosis of alveolar proteinosis was based on the positive staining of eosinophilic material in the alveolar space with a PAS reagent. Alveolar proteinosis was observed in the 1, 10 and 100 mg/m³ ITO-exposed rats and in the 10 and 100 mg/m³ IO-exposed rats, and its severity score was increased dose-dependently in both the ITO- and IO-exposed groups. Incidences of alveolar macrophage infiltration in the ITO and IO-exposed rats were increased at the same exposure concentrations as the occurrence of alveolar proteinosis. Infiltration of inflammatory cells which were primarily composed of neutrophils and lymphocytes was observed in the alveolar space and wall of almost all the 10 and 100 mg/m³ ITO- and IO-exposed rats of both sexes. Hyperplasia of alveolar epithelium occurred in some 10 and 100 mg/m³ ITO- and IO-exposed rats, and was characterized by increased numbers of cuboidal cells, which were assumed to be type II pneumocytes, and by their location in the focal lung areas accompanied by infiltrations of alveolar macrophages and inflammatory cells. Those alveolar macrophages had foamy cytoplasm.

Pathological findings in the 13-week study

Relative lung weights were significantly increased in all the rats of both sexes exposed to ITO and IO at 0.1 and 1 mg/m³ compared with the respective control groups (Fig. 2-B). The increase in the relative lung weight was more marked in the ITO-exposed rats of both sexes than in the IO-exposed rats. Increases in absolute lung weights were observed as well (data not shown).

Microscopic examination revealed that ITO and IO particles were deposited in the lungs of all the exposed

Table 3. Histopathological findings in the lung and lymph nodes of male and female rats exposed to ITO or IO at 4 different concentrations or clean air for 2 wk

	ITO					IO				
Group name (mg/m³)	Control	0.1	1	10	100	Control	0.1	1	10	100
No. of animals examined	5	5	5	5	5	5	5	5	5	5
<Male>										
Deposition of particles										
Lung	0	0	5	5	5	0	0	5	5	5
BALT	0	0	0	1	5	0	0	0	3	5
MLN	0	0	0	2	5	0	0	0	3	5
NALT	0	0	0	1	5	0	0	0	5	5
Histopathological findings										
Lung										
Alveolar proteinosis	0	0	5	5	5	0	0	0	5	5
			<1.0>	<2.0>	<2.0>				<1.8>	<2.0>
Infiltration of alveolar macrophages	0	0	5	5	5	0	0	0	5	5
			<1.0>	<1.0>	<1.0>				<1.0>	<1.0>
Infiltration of inflammatory cells	0	0	0	5	5	0	0	0	4	5
				<1.2>	<1.0>				<1.3>	<1.2>
Hyperplasia of alveolar epithelium	0	0	0	3	4	0	0	0	3	1
				<1.0>	<1.0>				<1.0>	<1.0>
<Female>										
Deposition of particles										
Lung	0	0	5	5	5	0	0	5	5	5
BALT	0	0	0	0	4	0	0	0	3	5
MLN	0	0	0	2	3	0	0	0	3	5
NALT	0	0	0	0	3	0	0	0	3	3
Histopathological findings										
Lung										
Alveolar proteinosis	0	0	5	5	5	0	0	0	5	5
			<1.0>	<2.0>	<2.0>				<1.8>	<2.0>
Infiltration of alveolar macrophages	0	0	5	5	5	0	0	2	5	5
			<1.0>	<1.0>	<1.0>			<1.0>	<1.0>	<1.0>
Infiltration of inflammatory cells	0	0	1	5	5	0	0	0	5	5
			<1.0>	<1.2>	<1.0>				<1.0>	<1.0>
Hyperplasia of alveolar epithelium	0	0	0	3	2	0	0	0	3	0
				<1.0>	<1.0>				<1.0>	

Values indicate number of animals bearing lesions. The values in angle bracket indicate the average of severity grade index of the lesion. The average of severity grade is calculated with a following equation. Σ(grade × number of animals with grade) / number of affected animals. Grade: 1, slight; 2, moderate; 3, marked; 4, severe. BALT: Bronchus-associated lymphoid tissue. MLN: Mediastinal lymph nodes. NALT: Nasal-associated lymphoid tissue.

rats of both sexes (Table 4). The particles were located primarily within the alveolar macrophages and partly as a free form within the alveolar space. ITO and IO particles were also observed to a lesser extent in the BALT of the 0.1 and 1 mg/m³ ITO- exposed and 1 mg/m³ IO-exposed rats, in the MLN of both 0.1 and 1 mg/m³ ITO- and IO-exposed rats, and in the NALT of the 1 mg/m³ ITO- and IO-exposed rats. Alveolar proteinosis occurred in all the ITO-exposed rats and in the 1 mg/m³ IO-exposed rats (Fig. 3-2). The severity score of alveolar proteinosis of the 0.1 mg/m³ ITO-exposed rats was equal to that of the 1 mg/m³ IO-exposed rats. Infiltration of alveolar macrophages was observed in the 0.1 and 1 mg/m³ ITO- and IO-exposed rats. Notably, swelling of cytoplasm in the alveolar macrophages was evidently recognized, indicating degeneration of the macrophages. Some alveolar macrophages contained PAS-positive, eosinophilic material in the cytoplasm. A significant increase in

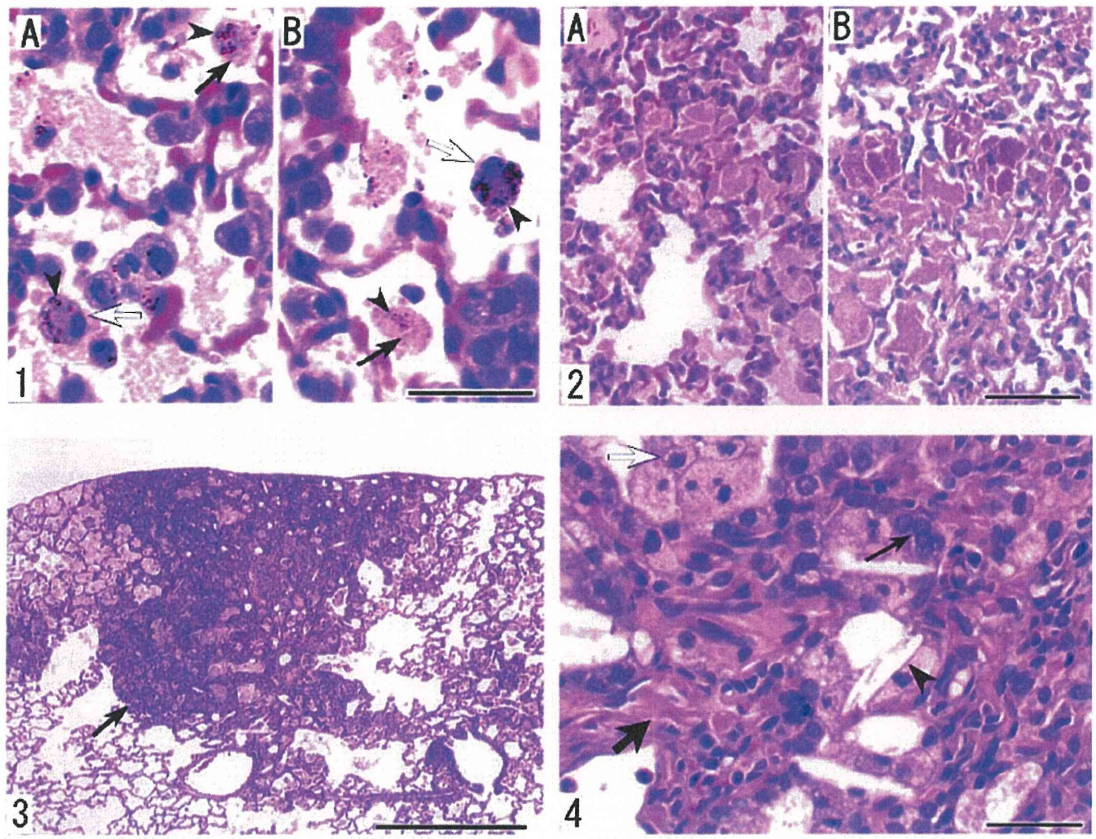

Fig. 3. 1) Microphotographs showing the presence of particles (arrowheads) in the alveolar macrophages in the lung of a male rat exposed to ITO at 100 mg/m^3 for 2 wk (A) and in the lung of another rat exposed to IO at 100 mg/m^3 for 2 wk (B). Note that alveolar macrophages engulfing the particles (open arrows) are degenerative (filled arrows). H & E stain. Bar indicates 50 μm. 2) Microphotographs showing alveolar proteinosis in the lung of a male rat exposed to ITO at 0.1 mg/m^3 for 13 wk, stained with H & E (A) and in the lung of the same rat stained with a PAS reagent (B). Bar indicates 100 μm. 3) A microphotograph showing a low power view of a focal lesion (arrow) located beneath the pleural wall in a male rat exposed to ITO at 0.1 mg/m^3 for 13 wk and then exposed to clean air for 26 wk. H & E stain. Bar indicates 500 μm. 4) A microphotograph showing a high power view of alveolar wall fibrosis, alveolar epithelial hyperplasia, and alveolar macrophage infiltration in a male rat exposed to ITO at 0.1 mg/m^3 for 13 wk and then exposed to clean air for 26 wk. Note the alveolar wall fibrosis indicating an increase in collagen-like connective tissue (thick filled arrow), hyperplasia of alveolar epithelium (thin filled arrow), cholesterol cleft (arrowhead) and swelling of cytoplasm in alveolar macrophages (open arrow). H & E stain. Bar indicates 50 μm.

inflammatory cell infiltration was observed in the 1 mg/m^3 ITO- and IO-exposed rats, and these incidences were higher in the ITO-exposed rats than in the IO-exposed rats. Hyperplasia of alveolar epithelium occurred mainly in some rats exposed to ITO at 0.1 mg/m^3 and in the 1 mg/m^3 IO-exposed rats. Small granulomas composed of particle-laden macrophages were observed in the MLN of the 0.1 and 1 mg/m^3 ITO-exposed rats and in the 1 mg/m^3 IO-exposed rats.

Pathological findings at the end of the 26-week post-exposure period

Relative lung weights were significantly increased in the exposed rats at the end of the 26-week post-exposure period as compared with those of respective controls (denoted as (P) in Fig. 2-B).

Microscopic examination revealed the presence of ITO particles in the lung, BALT and MLN of the exposed rats at the end of the 26-week post-exposure period (denoted as (P) in Table 4). All the lesions seen in the lung and lymph nodes/tissue of the 0.1 mg/m^3 ITO-exposed group at the end of the 13-week exposure period persisted throughout the 26-week post-exposure period. A focal lesion composed of alveolar wall fibrosis, alveolar epithelial hyperplasia, infiltrations of alveolar macrophages and inflammatory cells was observed beneath the pleural

Table 4. Histopathological findings in the lung and lymph nodes of male and female rats exposed to ITO or IO at 0, 0.1 or 1 mg/m³ for 13 wk, or exposed to ITO at 0.1 mg/m³ for 13 wk followed by exposure to clean air for 26 wk

	ITO					IO		
	13 wk			13 wk (P)		13 wk		
Group name (mg/m³)	Control	0.1	1	Control	0.1	Control	0.1	1
No. of animals examined	10	10	10	10	10	10	10	10
<Male>								
Deposition of particles								
Lung	0	10	10	0	10	0	10	10
BALT	0	9	9	0	7	0	0	10
MLN	0	7	9	0	9	0	0	10
NALT	0	0	2	0	0	0	0	2
Histopathological findings								
Lung								
Alveolar proteinosis	0	10 ** <2.0>	10 ** <3.0>	0	10 ** <1.7>	0	0	10** <2.0>
Infiltration of alveolar macrophages	0	10 ** <1.1>	10 ** <2.0>	0	10 ** <1.3>	0	6 * <1.0>	10** <1.0>
Infiltration of inflammatory cells	0	2 <1.0>	10 ** <1.0>	0	4 <1.0>	0	0	5 * <1.0>
Hyperplasia of alveolar epithelium	0	2 <1.0>	0	0	10 ** <1.3>	0	0	6 * <1.0>
Granuloma of BALT	0	0	1 <1.0>	0	0	0	0	0
Fibrosis of alveolar wall	0	0	0	0	10 ** <1.0>	0	0	0
Thickening of pleura	0	0	0	0	0	0	0	0
Lymph nodes								
Granuloma of MLN	0	5 * <1.0>	7 ** <1.0>	0	5 * <1.0>	0	0	5 * <1.0>

(P): Data at the end of the 26-week post-exposure period. Note: Values indicate number of animals bearing lesions. The values in angle bracket indicate the average of severity grade index of the lesion. The average of severity grade is calculated with a following equation. Σ(grade × number of animals with grade) / number of affected animals. Grade: 1, slight; 2, moderate; 3, marked; 4, severe. Significant difference: *, $p \leq 0.05$; **, $p \leq 0.01$ by Chi-square test. BALT: Bronchus-associated lymphoid tissue. MLN: Mediastinal lymph nodes. NALT: Nasal-associated lymphoid tissue.

wall (Fig. 3-3 and -4). Fibrosis of alveolar wall in all the exposed rats and thickening of pleural wall in one exposed female rat were evidently recognized only at the end of the 26-week post-exposure period, and were characterized by an increase in collagen-like connective tissue in the alveolar (Fig. 3-4) and pleural wall, respectively. It was noteworthy that cholesterol cleft (Fig. 3-4) was often observed in the same alveolar region at the end of the 26-week post-exposure period. The incidences and severities of alveolar epithelial hyperplasia were increased in the 26-week post-exposure groups as compared with that at the end of the 13-week exposure period.

No exposure-related histopathological changes were observed in any other organ or tissue in the ITO- or IO-exposed rats of either sex in the 2- and 13-week studies or at the end of the 26-week post-exposure period.

Discussion

The present system of aerosol generation and inhalation exposure was found to generate ITO and IO aerosols at the reproducible exposure concentrations regulated precisely within 10% coefficient of variation and accurately within 10% deviation from the target concentrations. Thus, this system allows to repeatedly expose individually housed, unrestrained rats of both sexes to ITO or IO particles of micron size at a wide range of concentrations from 0.1 to 100 mg/m³ in large inhalation exposure chambers (1 m³) for a time period of up to 90 days. The aerosols of ITO and IO in the exposure chamber were not aggregated and were well-dispersed to single particles of about 2–3 μm in

Table 4. continued

	ITO					IO		
	13 wk			13 wk (P)		13 wk		
Group name (mg/m³)	Control	0.1	1	Control	0.1	Control	0.1	1
No. of animals examined	10	10	10	10	10	10	10	10
<Female>								
Deposition of particles								
Lung	0	10	10	0	10	0	10	10
BALT	0	3	10	0	10	0	0	10
MLN	0	9	10	0	7	0	2	10
NALT	0	0	6	0	0	0	0	3
Histpothological findings								
Lung								
Alveolar proteinosis	0	10 ** <2.0>	10 ** <3.0>	0	10 ** <1.9>	0	0	10** <2.0>
Infiltration of alveolar macrophages	0	10 ** <1.0>	10 ** <2.0>	0	10 ** <1.5>	0	2 <1.0>	10** <1.0>
Infiltration of inflammatory cells	0	2 <1.0>	10 ** <1.0>	0	10 ** <1.0>	0	0	7 ** <1.0>
Hyperplasia of alveolar epithelium	0	5 * <1.0>	1 <1.0>	0	10 ** <1.4>	0	0	7 ** <1.0>
Granuloma of BALT	0	0	0	0	4 <1.0>	0	0	0
Fibrosis of alveolar wall	0	0	0	0	10 ** <1.0>	0	0	0
Thickening of pleura	0	0	0	0	1 <1.0>	0	0	0
Lymph nodes								
Granuloma of MLN	0	4 <1.0>	8 ** <1.0>	0	4 <1.0>	0	0	2 <1.0>

MMAD. The inhalation exposures of rats to the well-dispersed aerosols of ITO and IO resulted in depositions of ITO and IO particles in the alveolar region, which were detected in all exposed rats, except for those exposed to 0.1 mg/m³ for 2 wk. In addition, ITO and IO particles were deposited in the BALT, MLN and NALT of the exposed rats, but the extent of deposition was less in the lymph tissues and nodes than in the alveolar region. Light-microscopic examination of particle deposition in the lung and lymph nodes revealed that the particles were deposited separately as single particles.

It is interesting to note that the blood contents of indium in the male and female rats exposed to ITO at 1 mg/m³ for 13 wk were increased by 4.5- and 4.2-fold relative to the corresponding IO-exposed males and females, respectively, and that the blood contents of indium in the male and female rats exposed to 0.1 mg/m³ ITO were 0.77 and 1.13 $\mu g/l$, respectively, whereas the blood indium levels in the 0.1 mg/m³ IO-exposed rats of both sexes were below the detection limit of 0.5 $\mu g/l$. This finding can be interpreted as indicating that ITO particles are dissolved to greater extent in the deep lung than IO, resulting in higher blood contents of indium in the ITO-exposed rats. Kabe *et al.*[22] demonstrated that indium phosphide powder is clearly soluble in synthetic gastric fluid indicative of acidic pH, while the powder is insoluble in saline or synthetic lung fluid (Gamble solution). Dittmar *et al.*[23] reported that when indium phosphide particles are exposed to Gamble solution, a complex dynamic interaction with the particle surface results in high levels of dissolved indium. Brain *et al.*[24] suggested that insoluble metal particles contained in phagolysosomes of an alveolar macrophage are dissolved, because of the acidic environment (pH–4.8) in the phagolysosomes. The enhanced solubility of ITO particles in alveolar macrophages of the ITO-exposed rats warrants a further study.

The elemental or ionic form of indium leached from ITO particles is considered to play an important role in the induction of indium toxicity. Suzuki and Matsushita[25] showed that interaction of various metallic ions with surface pressure of phospholipid monolayer mimicking a biomembrane is positively correlated with acute lethal